University of Alberta

Utilizing Positron Emission Tomography to Detect Functional Changes Following Drug Therapy in a Renal Cell Carcinoma Mouse Model

by

David William Chapman

A thesis submitted to the Faculty of Graduate Studies and Research in partial fulfillment of the requirements for the degree of

Master of Science
in
Experimental Surgery

Department of Surgery

Spring, 2013
Edmonton, Alberta

Dedication

This thesis is dedicated to my Grandma Donna Chapman, and my close friend W. Owen Schlosser, who sadly passed away from cancer. Their passing inspired me to get involved in cancer research and they continue to motivate me on a daily basis.

I would also like to thank my parents, Matthew and Laura Chapman, and my grandparents, William and Shirley Lakey and Jack Chapman, for their love and support.

Furthermore, I would like to give special thanks to my mentors that continue to inspire me to achieve my goals. These include:

Dr. Jonathan Lakey for sparking my interest in basic science and giving me my first opportunity to get involved in cutting edge medical research. It has been a privilege to learn from you and I appreciate all of the opportunities that you have provided me with.

Dr. Branko Braam for selecting me as a summer student, and providing the opportunity to study renal cell carcinoma patient outcomes following surgical intervention and to compose my first few publications. This opportunity eventually led to basic research of RCC with Dr. Ronald Moore.

Abstract

Sunitinib is currently the first line drug therapy for metastasizing renal cell carcinoma (RCC). It has been shown to have a profound effect on tumor angiogenesis leading to modifications of the tumor's microenvironment. Tumor hypoxia plays an important role in the metastatic potential of a solid tumor and its resistance to any chemotherapy. Therefore, monitoring tumor hypoxia could potentially be used to detect and analyze therapeutic response. The present study utilized Positron-Emission Tomography (PET) to determine changes in tumor oxygenation during and following sunitinib therapy in a mouse RCC tumor model. Uptake of [^{18}F]FAZA tended to decrease during therapy of sunitinib, indicating a decrease in the tumor's hypoxia. However, after stopping drug therapy in tumor-bearing mice, this effect was reversed and tumor hypoxia was increased. [^{18}F]FAZA could potentially be used to monitor drug response of sunitinib therapy for RCC.

Acknowledgements

I would like to take this opportunity to give a heartfelt thank you to my supervisor, Dr. Ronald Moore, for his guidance in the completion of this project and further directing me towards a career in medical sciences. I feel very fortunate to have had the chance to observe the practices of an exceptional physician-scientist and mentor, and I have learned many things that I will take with me in the future.

This work could not have been completed without the help of Dr. Melinda Wuest. I thoroughly enjoyed conducting experiments with you and learning the “German way”. Thank you for all of your support. It has been a pleasure working with you.

Thank you to my Examining Committee, including Dr. Leonard Wiebe, Dr. John Mercer and Dr. Roger Zemp for the expert advice and support you have provided, allowing me to complete this project.

Furthermore, I would like to thank those who assisted me throughout my project including:

Ivy Ma- Moore Lab
Jacob Moibi- Moore Lab
Jimmy Xiao- Moore Lab
Cindy Johns- Administrative support
Christina Smith-Administrative support
Dr. Thomas Churchill- Graduate Coordinator
Brendan Trayner- Cell experiments
Monica Wang- Cell experiments
Anne Galloway- Administrative support
Ali Akbari- [^{18}F]FAZA synthesis
Blake Lazurko and David Clendening- Cyclotron Crew
Gail Hipperson, Dan McGinn, Daming Li- Vivarium

This work was financially supported by:

Mr. Lube Chair in Uro-oncology
Faculty of Medicine and Dentistry
Department of Surgery

Table of Contents

List of Figures

List of Abbreviations

ADP	Adenosine diphosphate
Ang	Angiopoietin
ATCC	American Type Culture Collection
ATP	Adenosine triphosphate
BCA	Bicinchoninic acid
ccRCC	Clear cell renal cell carcinoma
CT	Computed-tomography
Cu(II)-ATSM	Cu(II)-diacetyl-2,3-bis(N4-methyl-3-thiosemicarbazone
CYP	Cytochrome P450
Dll4	Delta-like ligand-4
DMSO	Dimethyl sulfoxide
ECM	Extracellular matrix
EGF	Epidermal growth factor
ERK	Extracellular signal receptor kinase
FAK	Focal adhesion kinase
[^{18}F]FAZA	[^{18}F]Fluoroarabinofuranosyl-2-nitroimadazole
[^{18}F]FDG	[^{18}F]-fluoro-2-deoxy-2-glucose
FLK-1	Fetal liver kinase
FLT-4	Fms-related tyrosine kinase-4
[^{18}F]FMISO	[^{18}F]Fluoromisonidazole
[^{18}F]EF5	[^{18}F]2-(2-nitro-1*H*-imidazole-1-yl)-*N*-(2,2,3,3,3-[^{18}F]pentafluoroproply)-acetamide
GIST	Gastrointestinal stromal tumors
Glut-1	Glucose transporter 1

HIF	Hypoxia-inducible factor
HIV	Human immunodeficiency virus
HRP	Horseradish peroxidase
$[^{124}I]$IAZA	$[^{124}I]$Iodoazomycin arabinoside
ICE	Interleukin-1 β-converting enzyme
IL-2	Interleukin-2
JAK	Janus kinase
KDR	Kinase insert domain receptor
MAP	Maximum a posteriori
MAPK	Mitogen-activated protein kinase
MDR-1	Multi-drug resistant transporter
MEK	Mitogen-activated protein kinase kinase
MHC-1	Major histocompatibility complex-1
MISO	Misonidazole
MMP-9	Metalloproteinase-9
mRCC	Metastatic renal cell carcinoma
MRI	Magnetic resonance imaging
NK	Natural killer
NRP-1	Neuropilin-1
OSEM	Ordered Subset Expectation Maximization
PDGF	Platelet-derived growth factor
PDGFR	Platelet-derived growth factor receptor
PET	Positron emission tomography
PI3-K	Phosphatidylinositol-3 kinase
PKB	Protein Kinase B
PLC-γ	Phospholipase C-γ
PTEN	Phosphotase and tensin homolog

RCC	Renal cell carcinoma
ROI	Region of interest
RTCC	Renal transitional cell carcinoma
RTK	Receptor tyrosine kinase
SEM	Standard error of the mean
SH2	Src Homology 2
SOCS	Suppressor of cytokine signaling
SPECT	Single photon emission computed tomography
STAT	Signal transducer and activator of transcription
SUV	Standardized uptake value
TAC	Time-activity curve
TGF	Transforming growth factor
Tie-2	Tyrosine kinase with immunoglobulin-like and EGF-like domains
TK	Tyrosine kinase
TKI	Tyrosine kinase inhibitor
TNM	Tumor-node-metastasis
tPA	tissue plasminogen activator
TSG	Tumor suppressor gene
uPA	Urokinase-type plasminogen activator
US	Ultrasonography
VEGF	Vascular endothelial growth factor
VEGFR	Vascular endothelial growth factor receptor
VHL	Von Hippel Lindau

Chapter 1: Introduction

1.1 Overview:

Renal cell carcinoma (RCC) has an incidence of 209,000 new cases and 102,000 deaths per year worldwide.[1] Treatment of RCC has evolved over the past few decades in regards to the methods of surgical intervention, approaches for the management of metastatic disease, and increasing consideration for the maintenance of renal function and co-morbidities before and after tumor resection.[2,3] There has been a shift from the use of relatively ineffective chemo-, radio-, and immuno-therapeutics to a more promising use of targeted therapies including anti-angiogenic drug therapy. For the latter purpose several tyrosine kinase inhibitors (TKI's) have been explored, both as single agents, and in combination therapies with other agents for the treatment of RCCs.[4] TKI's have previously been shown to lead to changes in vascular density followed by a modification in the tumor's microenvironment, namely oxygenation, and increasing necrotic regions.[5,6] The goal of this project was to utilize positron emission tomography (PET) for the analysis of functional changes in the tumor's microenvironment in a RCC mouse model after therapy with the TKI inhibitor sunitinib.

1.2 Renal Cell Carcinoma of the Kidney

1.2.1 Kidney Function

The kidney is the main clearance organ for the renal elimination pathway in the human body. Its main function includes removal of many compounds from the human physiological processes, balance of electrolytes and pH, regulation of blood volume and pressure, as well as stimulation of red blood cell production.[7] The kidneys are able to perform these functions by three main processes including filtration, secretion, and reabsorption. The first process, filtration, plays an important role of removing plasma proteins, cells, and other macromolecules that cannot pass through the glomerulus. Filtration is driven by Starling forces, the net result of hydrostatic and oncotic pressure. The filtrate then passes through the proximal convoluted tubule and the loop of Henle, where it reaches the collecting duct to form urine for the final excretion. Reabsorption includes removal of water and solutes from the tubular fluid and transport of it to the blood. These functions are essential to maintain steady-state levels of solutes, water, and hormones in the blood. The most important process in the context of any pharmaceutical drug or injected radiotracer (if renal clearance is the most predominant excretion pathway) is secretion. Many compounds are secreted from the peritubular capillaries to the tubules where they are excreted into the urine. Overall the renal clearance is an important body function and more importantly, the renal clearance of radiotracers can interfere with certain types of renal imaging.

1.2.2 Renal Cell Carcinoma (RCC)

1.2.2.1 Epidemiology

Cancers can arise from the kidney's parenchymal tissue, including the medulla and cortex tissue, and the collecting system, which includes the renal pelvis. In comparison to renal transitional cell carcinomas (RTCC) that develop from the collecting system, adenocarcinomas such as renal cell carcinoma (RCC) are formed from parenchymal tissue of the kidney.[7] RCC is the most common type of kidney cancer, affecting 2-3% of all malignant diseases in adults and accounting for more than 90% of adult kidney carcinomas.[7,8]

The National Cancer Institute has estimated that there were 64,770 new cases and 13,570 deaths in the United States in 2012, as compared to the 2005 prediction statistics of 36,160 new cases and 12,660 deaths.[9,10] There has been a steady increase in incidence rates for renal cell carcinoma that can be attributed to the overall increasing life expectancy and advances in diagnostic tools such as non-invasive imaging techniques that allows visualization of much smaller lesions and therefore diagnosis at much earlier stages.[11]

Both sporadic and familial forms of renal cancer occur and can exist as several different tumor types including clear-cell RCC, papillary RCC, oncocytoma and chromophobe RCC, and collecting duct RCC.[12] There are several classical environmental factors that are directly linked to incidence and mortality rates, including cigarette smoking status, obesity, diabetes, and physical inactivity.[13-16] Hypertension, rather than anti-hypertensive or diuretic drugs, is considered an independent risk factor for renal cell cancer as well.[12,17] There are also a number of western dietary factors that are currently being investigated including protein, fat, and meat consumption (all meat, red meat, processed meat); however, no conclusive results have been made yet.[12,18] A unique finding by J.E. Lee *et al.* has shown that moderate alcohol consumption, defined as slightly more than one drink per day, was associated with a decreased risk of renal cell cancer.[19] Other protective factors for RCC include oral contraceptive use, increased consumption of fruits and vegetables, and greater physical activity.[20,21]

Along with these environmental risk factors, several genetic factors have been shown to contribute to the incidence of RCC. Patients with “Von Hippel Lindau (VHL) Syndrome”, an autosomal dominant disorder characterized by the loss of VHL tumor suppressor gene (TSG), are at substantial risk to develop benign and malignant tumors in several different organ systems, including the central nervous system, kidneys, adrenal glands, pancreas and reproductive organs.[7,22] More specifically, the loss of VHL TSG in “Von Hippel Lindau Syndrome” makes individuals more susceptible to the clear cell subtype of RCC and they often present with bilateral or multiple renal lesions.[7,22] Patients with VHL syndrome need to be closely monitored by urologists in order to detect early stage renal tumors. Another form of the hereditary papillary RCC can result from a point mutation in the tyrosine kinase domain of the c-MET proto-oncogene that encodes a protein called hepatocyte growth factor receptor, accounting for about 5-13% of papillary (type I) RCC’s.[23] Inactivating mutations in fumurate hydratase tumor suppressor gene, an enzyme of the “Krebs cycle”, can also result in a rare form of papillary (type II) RCC.[24] Although these hereditary kidney cancers are not the most prevalent ones, they can serve for a specific analysis of the underlying mechanisms of cancer formation, allowing the identification of novel targets for anti-cancer therapy.

1.2.2.2 Staging of RCC

Similar to other malignant diseases, the prognosis of the patient is dependent on the size, localization of the tumor and the presence of metastasis. Since there are no laboratory (blood, urine) screening parameters for indicating the presence of renal cell carcinoma, it is difficult to identify it at an early stage with a favorable prognosis, except for incidental radiological detection. Since the presentation of the symptoms of RCC often appear too late, incidental detection of RCC tumors gives patients a significant advantage. As non-invasive imaging technology continues to improve, earlier detection of tumors is possible. Unfortunately, the increased incidence of renal cell carcinoma is not only attributed to improved detection but also to increased prevalence of the disease.[25] Magnetic resonance imaging (MRI), computed-tomography (CT), ultrasonography (US), and positron emission tomography (PET) are non-invasive imaging methods, which can be used for the detection of renal cancers.[26] Following initial diagnosis, the tumor needs to be staged in order to guide patient therapy. The current staging method utilizes the following three parameters and is defined as TNM staging (T=primary tumor, N= regional lymph nodes, M= distant metastasis).[27] A suitable staging method for malignant disease must have the ability to assist the physician in making treatment decisions, as well as provide information that will allow an accurate prognosis to be made. This need is reflected in the constant evolution of the TNM staging method into further stratification of the stages as a greater understanding of the disease is developed. Most alterations have occurred in primary tumor staging where significant clinical differences in patient stratifications have occurred over time. In the older TNM system; T1 were tumors with diameter < 2.5 cm confined to the organ, T2 for tumors > 2.5 cm confined to the organ, T3a for tumors extending out to perinephric tissue or contiguous into adrenal gland, T3b for renal vein involvement, T3c for vena cava tumor involvement below diaphragm, and T4 for tumors beyond Gerota's fascia or vena cava above diaphragm.[28] Recently in 2010, there have been several sub-stages added: T1 tumors have been sub-divided into both T1a (≤4 cm), and T1b (4-7 cm), T2a (7-10 cm), T2b (> 10cm, all organ confined), T3a for involvement of paranephric tissue, renal sinus, or renal vein, T3b for vena cava involvement below the diaphragm, T3c for involvement in vena cava above diaphragm or into wall of vena cava at any level, and T4 for any tumor beyond Gerota's fascia or directly into adrenal gland.[28]

1.2.2.3 Treatment Options

Following the diagnosis of small renal lesions, a very important decision needs to be made for the surgical treatment of individual patients. In the past, patients would frequently undergo a radical nephrectomy without the consideration of the more conservative alternative, a partial nephrectomy. It has been found that similar oncological outcomes result from both partial and radical nephrectomy for the treatment of small renal masses without metastasis, prompting urologists to take into consideration other factors including renal function.[29] Some of these other factors include tumor stage (based on size), localization of the tumor within the kidney (nephrometry), expertise of the surgeon, and patient conditions such as contralateral kidney function and ability to compensate for renal loss, as well as co-morbidities.[30] Prior to surgical intervention, certain patients should be referred to a nephrologist in order to improve pre-surgical renal function, and to risk stratify to establish limitations for surgical intervention (for example, advise or for radical/partial nephrectomy or observation) in order to maintain sufficient renal mass.[30]

Often RCC is not detected until late, when symptoms are presented and a favorable prognosis is less likely. Management of metastatic RCC (mRCC) also requires more than surgical excision. Currently there is no single pharmaceutical drug available that can suppress renal tumor cell growth completely. This results in longer chronic treatment and overall long-term drug therapy burden with all its expected side-effects.[8] Spontaneous regression of the metastatic disease following radical or partial nephrectomy is a unique characteristic of RCC, leading clinicians and researchers to focus on patient immunotherapy.[31] Interferon-α, in addition to possessing anti-viral properties, has the ability to cause anti-proliferative effects on cells.[32] The mechanism of action is not fully understood yet and response to this compound is highly variable between patients, as shown by the response rates ranging from 4% to 26%.[33] Interferon-α acts both directly on the tumor, and indirectly via the host immune cells. Directly, interferon-α can induce tumor suppressor genes and down-regulate oncogene expression, as well as enhance immune recognition through increased major histocompatibility complex-1 (MHC-1) expression.[34] Interferon-α can also mediate its direct anti-proliferative effects by regulating tumor necrosis factor-induced signaling.[35] Indirectly, interferon-α is involved in the modulation of T-cell response through several different interactions including the role as a differentiation signal for precursor cells becoming cytotoxic T lymphocytes.[36,37] Another cytokine commonly used in patients with renal cell carcinoma is interleukin-2 (IL-2). IL-2 was found to increase the number of cells positive for Leu11 antigen, a protein indicative of natural killer (NK) cells of the innate immunity.[38] High doses of IL-2 produce modest response rates of 15-20%, however, it is associated with severe toxicities.[39] Although the overall response and survival rates of patients administered with either IL-2 or interferon-α offered some benefits in RCC management, researchers began investigating the use of these compounds as combination therapy, and also in combination with other classes of drugs. However, in combination with each other, IL-2 and interferon-α did not show significant improvements over single agent treatment in patients with advanced RCC when administered intravenously.[40] Ravaud *et al.* found that the subcutaneous administration of IL-2 and interferon-α combination therapy showed indications of lower efficacy and higher toxicity rates than intravenous administration.[41] Although other studies found that some patients are likely to benefit from IL-2 / interferon-α immunotherapy, further research is required to analyze the variables behind these favorable responses.[42]

Drug resistance has played a significant role in the inability of both of these agents to produce durable and complete responses. Interferon-α, for example, plays an important role in the Janus kinase/signal transducer and activator of transcription (JAK/STAT) pathway.[43] Like in all signaling pathways, the intricate balance between inducers and suppressors controls signal transduction. Interferon-α mediated JAK/STAT signaling has been shown to be inhibited by subtypes of the suppressor of cytokine signaling (SOCS) protein family, mainly SOCS1 and SOCS3. These proteins are found to be over-expressed following interferon-α treatment, and are believed to play a key role in limiting its efficacy.[35] Tomita *et al.* also found that inhibiting SOCS3 protein restored sensitivity to interferon-α therapy.[35] Additionally, resistance to conventional chemotherapy can also occur due to over-expression of multi-drug resistant transporter (MDR-1/P-glycoprotein), which acts to pump chemical compounds out of renal tubular and tumor cells, resulting in a poorer clinical prognosis.[44] From the investigation of a wide selection of drugs as either single or combined agents, it was apparent that novel approaches for drug treatment of metastatic RCC were needed and the focus shifted to targeting mechanisms utilizing new chemical entities. This has led to the development of a new class of small molecules, the tyrosine kinase inhibitors.

1. 3 Tumor Angiogenic Pathways

1.3.1 Angiogenesis

As outlined by Hanahan and Weinberg, sustained angiogenesis is one of the essential hallmarks that drives tumorigenesis.[45] As tumors grow, the increased metabolic demand exceeds the supply of oxygen and other nutrients, leading to more aggressive and increasingly malignant cells.[46] Cells undergo metabolic changes in order to survive under such specific conditions. Angiogenesis is driven mainly by the master transcription factor, hypoxia-inducible factor (HIF). HIF-1α levels are controlled by the oxygen tension within the cell. More specifically, under hypoxia, HIF-1α is activated and leads to the production of proteins essential for angiogenesis, the formation of new vessels (see Figure 1).

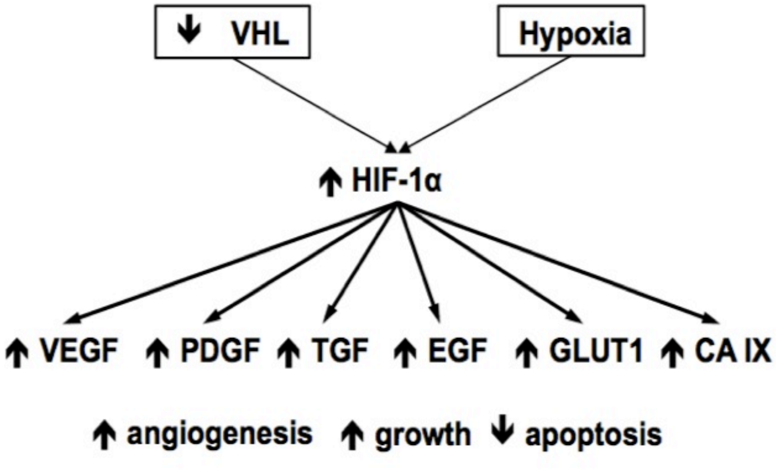

Figure 1: Master Transcription factor, HIF-1α, and its downstream targets

This makes angiogenesis an excellent process to target in order to impede tumor growth. The process of angiogenesis is very complex and is tightly regulated by the simultaneous activation of both anti- and pro-apoptotic signals in order to develop proper vessels.[47] There are four important pathways involved in angiogenesis including the (i) VEGF-A/VEGFR2 pathway, (ii) angiopoietin/Tie2 (tyrosine kinase with immunoglobulin-like and EGF-like domains) pathway, (iii) DII4(delta-like-ligand 4)/Notch1 pathway, and (iv) the PDGF-B/PDGFR-β (platelet derived growth factor receptor) pathway, all representing several potential targets for therapeutic interventions (see Figure 2).[47] A requisite for the formation of new blood vessels is the binding of VEGF-A to VEGFR-2, VEGFR-1 and Neuropilin.[47] Following the initiation of vessel formation by VEGF-A binding, among other processes, is the involvement of angiopoietins (Ang). As summarized by Roodink *et al.,* binding of Ang to Tie2 receptor, another endothelial cell specific tyrosine kinase (TK) receptor, causes autophosphorylation and promotion of angiogenesis.[48] Although Ang-1/Tie2 is not involved in initiation of angiogenesis, this pathway is necessary for supporting the newly forming vessels.[49] Two forms of Ang exist: Ang-1 and Ang-2. Binding of Ang-1 to Tie2 receptor leads to an agonistic activation and subsequent downstream effects, while Ang-2 acts antagonistically by completely blocking Tie2.[47] Activation of Tie2 resulting from Ang-1 binding leads to the recruitment of pericytes, which contributes to vessel stabilization and maturation of vessels.[50] Ang-2 plays an important role in the remodeling of blood vessels by inhibiting the interaction between supporting pericytes and vessels resulting in regression.[47] The Ang/Tie2 pathway involved in tumorigenesis has been explored as a potential target for inhibition by several groups.[49] Controversially, Ang-1 has been shown to inhibit vascular permeability, angiogenesis, and tumor growth.[51,52] These two opposing effects of Ang-1 may be due to the timing of its presence during the process of angiogenesis. During the initiation phase of angiogenesis Ang-1 may act antagonistically, and after the immature vessels have formed Ang-1 acts to promote vessel stability and maturation.

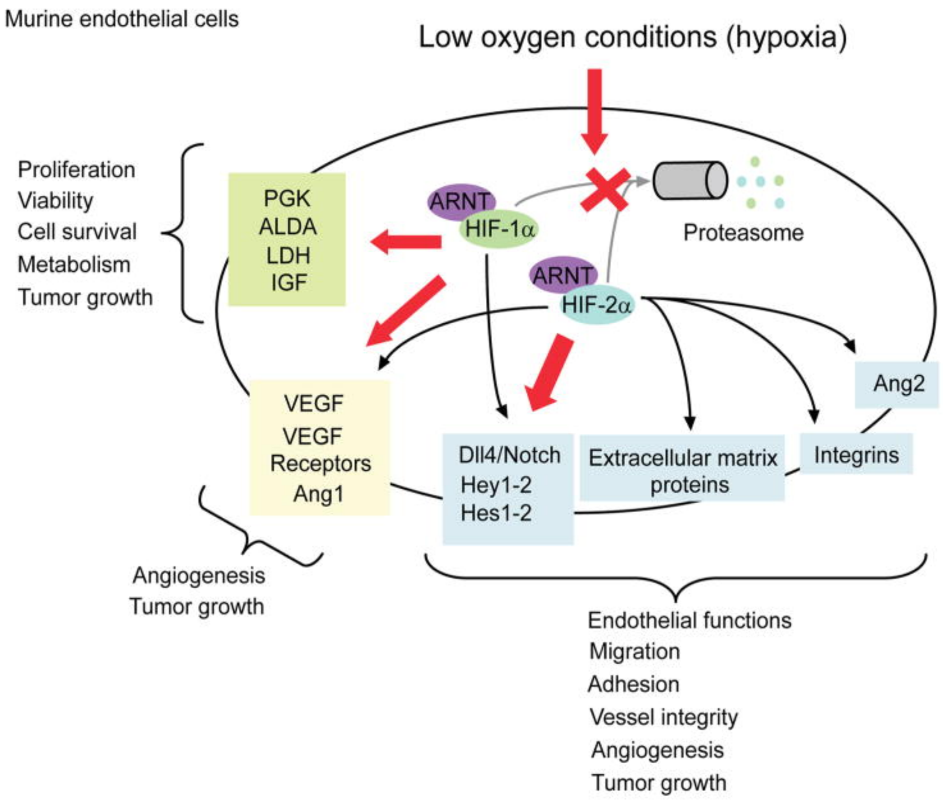

Figure 2: Induction of multiple downstream pathways in endothelial cells under low oxygen conditions.[53] ALDA, Aldehyde Dehydrogenase; IGF, Insulin Growth Factor; LDH, Lactate Dehydrogenase; PGK, Phosphoglycerate Kinase; ARNT, Aryl hydrocarbon nuclear translocator.

VEGF-A induced angiogenesis is also regulated by an additional pathway, the DII4/Notch1 pathway. An up-regulation of delta-like ligand-4 (DII4) expression on tip cells, cells present at the leading edge of vascular sprouts, occurs following the activation of angiogenesis by VEGF-A ligand binding.[47,54] Along with VEGF, the binding of Wnt proteins to frizzled family receptors activates catenin molecules, which translocate to the nucleus and increase DII4/Notch expression.[54] This leads to the activation of Notch receptors and in turn, down-regulates VEGFR-2 receptors on flanking endothelial cells and guides functional vessel development by avoiding chaotic branching.[47] Inhibition of the Notch pathway has been previously analyzed revealing a reduction in tumor growth.[55] Additionally, angiogenesis has been targeted for cancer therapy by inhibition of the PDGF-B and PDGFR-β pathway.[47]

1.3.2 Vascular Endothelial Growth Factors and Receptors

The family of vascular endothelial growth factors includes VEGF-A, VEGF-B, VEGF-C, VEGF-D, and placental growth factor, each with specific but also overlapping functions. VEGFs are potent, yet selective mitogens that signal for the promotion of both physiological and pathological angiogenesis and lymphogenesis.[56,57] VEGF is thought to play a critical role in the rate-limiting step of angiogenesis.[58]

VEGF-A, the first of the VEGF cytokines to be studied, is expressed in solid tumors and signals for angiogenesis mainly through VEGF receptor-2/Fetal liver kinase (FLK-1) /Kinase insert domain receptor (KDR) found on vascular endothelial cells.[57] VEGF_{121} is freely diffusible and is secreted from the tumor cell, while the isoforms VEGF_{189} and VEGF_{206} are held in the extracellular matrix (ECM) of the tumor cell, only to have a diffusible bioactive fragment released by C-terminus plasmin cleavage.[58] VEGF_{121} is also unique because it does not bind to heparin, like the other isoforms. VEGF_{165} shares properties of both VEGF_{206} and VEGF_{189} where one small fragment is secreted and the larger fragment remains bound to the ECM.[58] Along with binding to VEGFR2 receptors, VEGF-A can also exert its effects by binding to integrins.[59] This additional mechanism may serve as another target for inhibiting angiogenesis. Conversely, VEGF-C promotes lymphogenesis, the formation of lymphatic vessels by targeting VEGFR-3/FLT-4, a receptor found on lymphatic endothelial cells. VEGF has been shown to increase permeability of capillary beds, as well as cause fenestrations to form in the endothelial cells of blood vessels.[60] VEGF is also believed to cause an increase in hexose transport, which may serve to assist with the higher than normal energy demand during endothelial and tumor/stromal cell proliferation.[61]

VEGF binds to cell surface receptors, the VEGF receptors (VEGFR). VEGFR's are expressed on the cellular surface of endothelial and bone marrow derived cells such as monocytes.[58] VEGFR-1, VEGFR-2 and VEGFR-3 belong to the receptor tyrosine kinase (RTK) family. VEGFR-3 is a target for VEGF-C and VEGF-D ligands and is thought to be involved in the process of lymphogenesis and lymphatic metastasis (*vide-supra*).[62] Binding of VEGF-A, VEGF-B and placenta growth factor to VEGFR-1 results in a number of specific effects (see Figure 3). One such effect, defined as the "decoy effect", occurs when VEGFR-1 acts as an inert binding site that negatively modulates VEGFR-2 signaling and endothelial cell proliferation by sequestering VEGF.[58] On the other hand, placenta growth factor binding to VEGFR-1 increases angiogenesis and synergism with VEGF.[63] Other effects of binding to VEGFR-1 include the induction of urokinase-type plasminogen activator (uPA), tissue plasminogen activator (tPA), and matrix metalloproteinase-9 (MMP-9). MMP-9 has been shown to play a crucial role in the "angiogenic switch" during carcinogenesis.[64] The angiogenic switch is defined as an event that occurs when the balance of pro- and anti-angiogenic factors is in favor of pro-angiogenesis, leading to the development of a highly vascularized tumor and eventually malignancy.[65] VEGFR-2, also named the kinase domain region (KDR) or fetal liver kinase-1 (Flk-1), is the main receptor for angiogenesis and permeability-enhancing effects of VEGF.[58] VEGF-A has been shown to bind to neuropilin (NRP-1), a receptor that interacts with VEGFR-2, and potentiates its activity.[66]

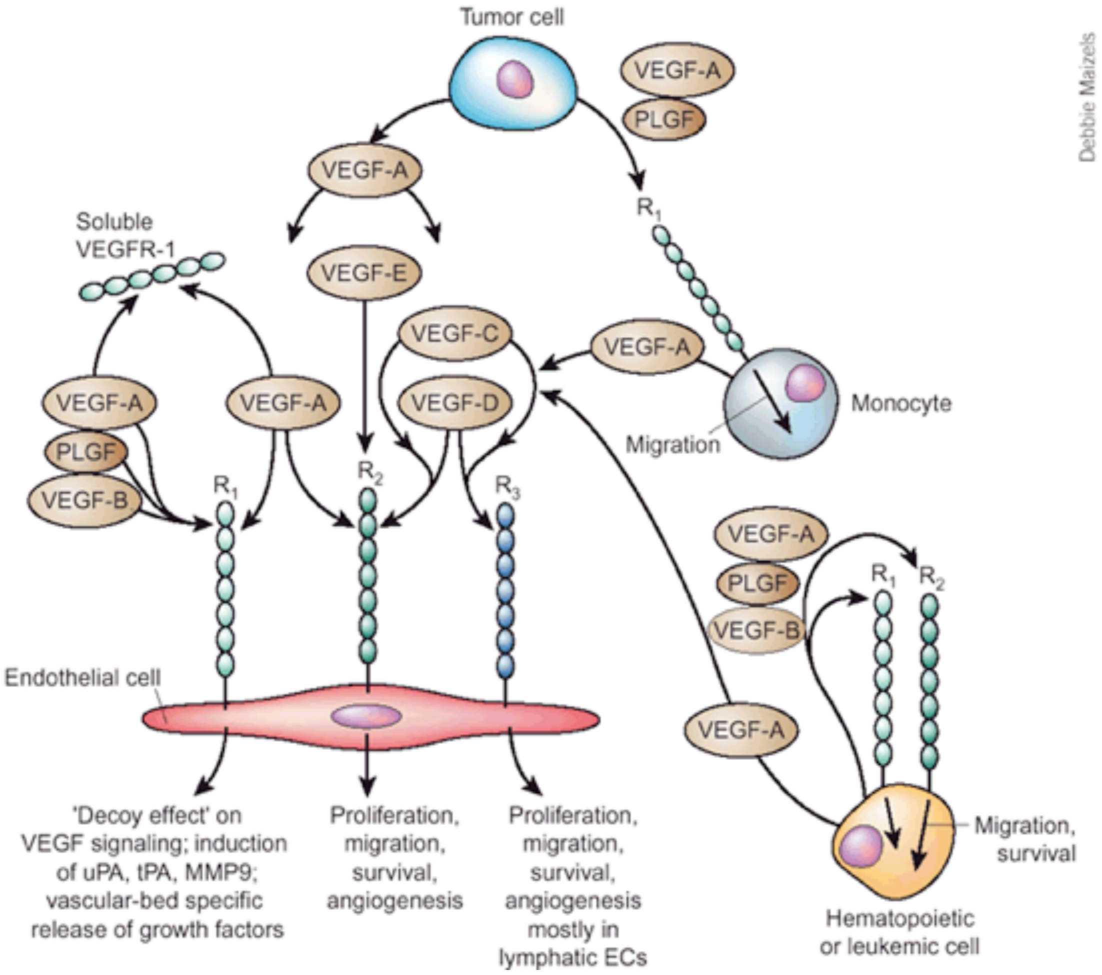

Figure 3: Different interactions between VEGF's and VEGFR's result in a wide variety of effects.[58]

1.3.3 Platelet Derived Growth Factor

In addition to VEGF, another important gene product driven by the HIF-1 transcription factor in response to hypoxia is the platelet-derived growth factor (PDGF).[67] The PDGF family also includes four different known factors, PDGF-A, -B, -C, and –D.[68] They all contain a growth factor core domain rich in cysteine residues that is necessary to bind and activate receptor tyrosine kinases. They all bind mainly to two receptor subtypes, PDGFR-α and PDGFR-β.[68] Further identified and discussed by Andrae *et al.* was the similarity of PDGF receptors to c-Fms, c-Kit), and fms-related tyrosine kinase receptor (Flt3).[68] Multiple receptors with similar structures may allow inhibition by the same chemical compound and play an important role in the development of novel multitargeting therapies for the treatment of cancers. Alternatively, this may result in additional toxicity from off-target effects. Like VEGF receptors, ligand binding to PDGF receptors results in dimerization, and signal transduction.[68] The activation of these receptors leads to the initiation of several cascades similar to VEGFR activation including PI-3K survival pathway.[68] PDGF-A isoform activation of α-PDGFR participates in biological processes including chemotaxis, anchorage-independent growth, and focus formation.[69] The activation of PDGFR-β leads to the initiation of several cascades similar to that of VEGFR's including PI-3K/Akt pathways, and the MAPK pathway, ultimately resulting in cell migration.[70] PDGF has also been shown to induce proliferation of smooth muscle cells by boosting rate of glycolysis and mitochondrial oxygen consumption.[71] PDGF, VEGF and other growth factors play a crucial role in tumorigenesis and angiogenesis in human cancers, making them key targets for drug therapy.

1.3.4 Tyrosine Kinase Signal Transduction

Mitogenesis

Following VEGF-A, C, D, and E ligand binding, phosphorylation of the tyrosine residues and subsequent dimerization occurs resulting in mitogenesis, migration via chemotaxis, and transduction of pro-survival signals (see Figure 4).[58] There are two pathways of mitogenic activation following ligand binding to receptor tyrosine kinases such as VEGFR. One pathway is the ras-dependent activation of ERKs (extracellular signal receptor kinases), and the other is ras-independent activation of ERKs via phospholipase Cγ (PLC-γ).[72] The first pathway, dependent on ras-activation acts through the Raf-1/MEK/ERK cascade, while the second less contributing mechanism involves PLC-γ phosphorylation.[72,73]

Migration

Cell migration is another result of VEGF substrate binding to RTK's. There are a number of pathways required for the migration of cells including VEGF activated RTK (VEGFR-2/KDR) and integrin-mediated, that both result in the activation of focal adhesion kinase (FAK).[72] It has been shown that binding of VEGF-A to integrin-$\alpha_9\beta_1$ resulted in endothelial as well as cancer cell migration.[59] The up-regulation of many of these signaling factors as a result of hypoxia leads to changes in the migratory behavior of cancer cells.

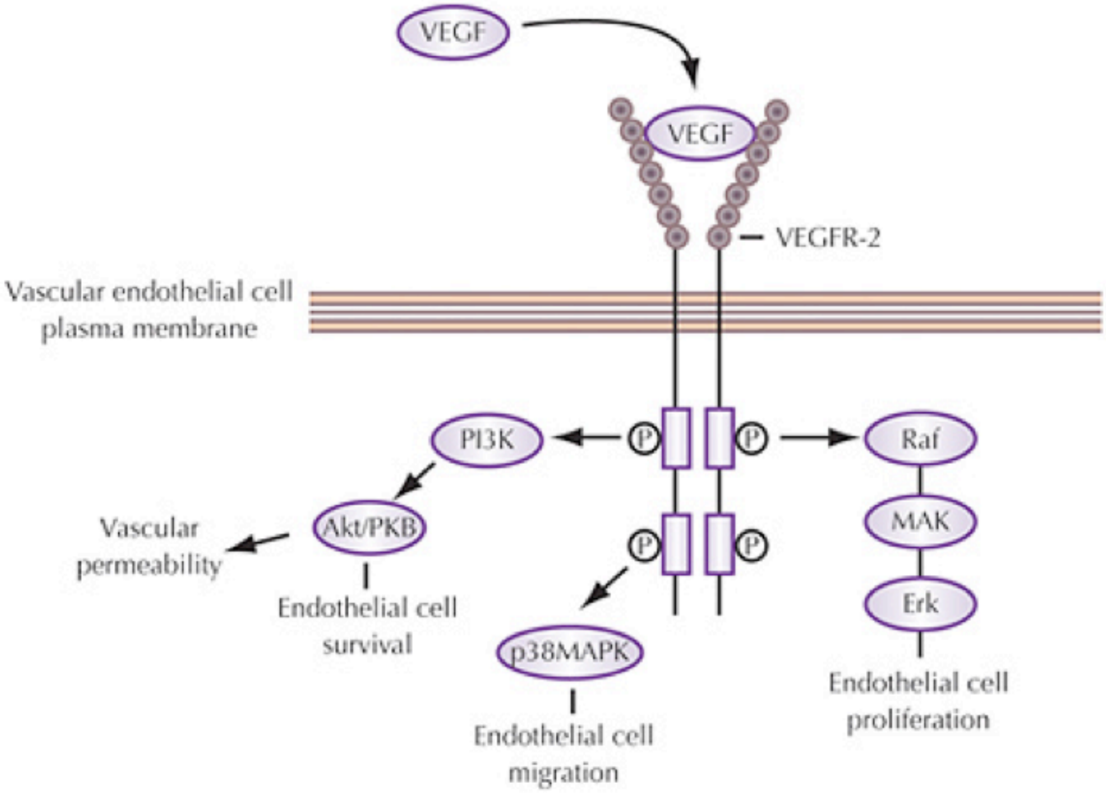

Figure 4: Multiple downstream pathway activation following VEGF binding to VEGFR2 [74]

Following integrin engagement at the cell surface, extracellular signals are projected to the cytoskeleton through the activation of the tyrosine kinase, FAK, by autophosphorylation, creating a binding site for Src Homology 2 (SH2) domains of several proteins (see Figure 4).[75,76] Src, a tyrosine kinase, is one such protein with an SH2 binding domain and activation has been shown to be associated with VEGF substrate binding to the VEGFR-2/KDR receptor.[75] In melanoma cells for example, inhibition of Src has been shown to block migration and invasion, while leaving proliferation and cell-survival intact, emphasizing Src's crucial role in migration pathways.[77] Following phosphorylation and activation of FAK, Src binds to form FAK/Src complex. Both FAK and Src become enzymatically active following the association with each other and can activate downstream cytoskeletal proteins, including tensin, paxillin and p130cas (a docking protein), through phosphorylation.[78] Phosphorylation of paxillin and p130cas has been shown to be important in the cell adhesion turnover, the process of forming and disassembling focal adhesions.[79,80] FAK has also been shown to activate downstream pathways including MAP kinase and PI3-kinase which are both known to play important roles in integrin-mediated cell adhesion.[78] Ultimately, the over activation of the MAPK cascade leads to changes in gene expression, mitosis, differentiation, proliferation and survival in many cancers.[81]

Survival

Survival mechanisms result from VEGF and other growth factor ligands as well as integrin binding. Specifically, environmental stressors, namely, hypoxia can induce VEGF to bind to VEGFR-2/KDR, activating phosphatidylinositol 3 kinase (PI3K), which leads to the recruitment of Akt/protein kinase B (PKB) to the plasma membrane. In turn, this brings Akt in close proximity to upstream kinases, which are then able to phosphorylate and activate Akt.[82,83] One mechanism through which cell death is **prevented** by Akt/PKB activation is the inhibition of the activities of Ced3/ICE (interleukin-1β-converting enzyme)-like proteases. Ced3/ICE-like proteases specifically cleave the poly (ADP-ribose) polymerase (PARP), leading to cell death.[84] Alternatively, activated Akt phosphorylates Bad, a bcl-2 family member that promotes apoptosis, sequestering it in the cytoplasm, and preventing the interaction between Bad and anti-apoptosis proteins such as bcl-xl and bcl-2.[85] Without Akt phosphorylation, Bad heterodimerizes with anti-apoptotic bcl-2 family proteins, including Bcl-xl, and renders them inactive.[83,86] Also, Akt prevents apoptosis through the activation of Nuclear Factor-κB (NFκB), a transcription factor that when activated, leads to increased expression of Bcl-xl, cell-cycle genes, surviving and invasion promoting proteases such as MMP-9.[87] Phosphatase and tensin homolog (PTEN) plays an important role in the regulation of apoptosis metabolism, cell proliferation and cell growth and a **loss** of PTEN function has been shown to be involved in the formation of many human cancers.[88,89]

1.4 Drug Therapy through Angiogenesis Pathways

1.4.1 Tyrosine Kinase Inhibitors

Kinases are enzymes that transfer phosphate groups from high-energy donors such as adenosine triphosphate (ATP) to other proteins which alter structural conformation and activity resulting in signal transduction.[90] Tyrosine kinases exist in two forms, receptor tyrosine kinases which transduce signals from outside of the cell to the inside and non-receptor tyrosine kinases which are found within the cell in the cytoplasm.[90] Receptor tyrosine kinases consist of three components: an N-terminal extracellular ligand-binding domain, a transmembrane domain, and a C-terminal intracellular domain that possess tyrosine kinase activity.[90] Dimerization of receptor monomers occurs after ligands bind to the extracellular domain. Following dimerization, autophosphorylation of tyrosine residues occurs, inducing changes in the conformation of the activation loop allowing interaction with different proteins.[91]

Currently, seven different drugs have been shown to have efficacy in the treatment of metastatic renal cell carcinoma, four of which are tyrosine kinase inhibitors namely sunitinib, sorafenib, pazopanib and axitinib.[92] Two types of tyrosine kinases inhibitors exist, including Type I, and Type II inhibitors. Type I inhibitors act specifically at the ATP-binding site by forming hydrogen bonds that mimic the bonds normally formed by ATP, essentially acting as an ATP analogue.[93] Sunitinib is an example of a type I tyrosine kinase inhibitor, and is currently approved for the treatment of metastatic renal cell carcinoma, and gastrointestinal stromal tumors (GIST).[94] Conversely, type II tyrosine kinase inhibitors indirectly inhibit ATP binding by interacting with the hydrophobic pocket that is directly adjacent to the ATP-binding site.[90] Sorafenib, axitinib, and pazopanib are examples of a type II tyrosine kinase inhibitors (see Figure 5).[90]

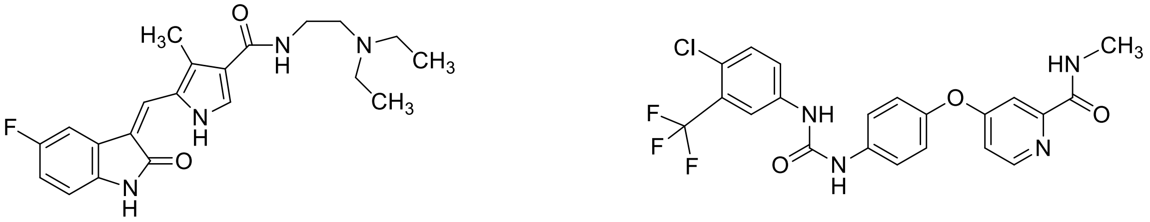

Sunitinib

Sorafenib

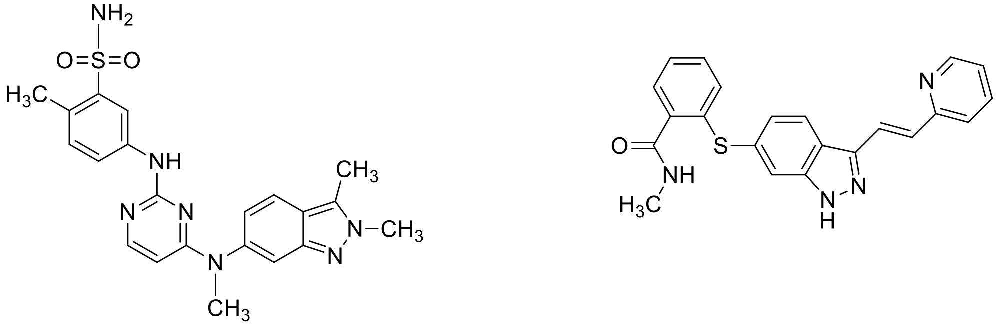

Pazopanib

Axitinib

Figure 5: Tyrosine kinase inhibitors approved by the FDA for the treatment of renal cell carcinoma (Status year 2012)[87]

1.4.2 Sunitinib

Sunitinib is currently the first-line therapy for the treatment of metastatic renal cell carcinoma (RCC). It is taken orally at a dose of 50 mg daily for four weeks in a row following a two week rest period.[95] Sunitinib (Sutent®) is a multi-targeting tyrosine kinase inhibitor (TKI) approved for the treatment of many malignant cancers including GIST and RCC, and is still being investigated for use in several other types of cancer.[96,97] It acts to impede the process of tumor growth, progression and metastasis by disrupting the autophosphorylation of RTKs and downstream tyrosine kinases.[98] It has been proposed that through inhibition of ATP binding, sunitinib blocks the autocrine kinase activity following ligand binding.[98] Furthermore, Adams *et al.* summarized that sunitinib acts on multiple targets to inhibit VEGFR 1, 2, 3, PDGF α and β, c-kit, Fms-like TK-3 (FLT3), colony-stimulating factor receptor type 1 and neurotrophic factor receptor.[98,99] As previously mentioned, inhibition of these receptors leads to the blockage of downstream signaling, ultimately increasing rate of apoptosis, and reducing angiogenesis, tumor cell invasion and metastasis.[96,98] One study stated that sunitinib acts both directly on the tumor cells (GIST and RCC), and also indirectly by disrupting the development of blood vessels, causing increased microenvironmental stress on the tumor tissue.[98] Conversely, a different study found that sunitinib acts primarily through the endothelial cells, and not through targeting receptors on clear cell RCC (ccRCC) cells.[100] Additionally, it has also been proposed that sunitinib plays an immunomodulatory role by improving type-1 T-cell cytokine response and reducing T regulatory cells.[101] As immune dysfunction is commonly found in patients with RCC, this may play an important role in treatment by rallying the involvement of the immune system to assist the tumor growth inhibitory properties of sunitinib. Following orally administered sunitinib, the bioavailability does not seem to be affected by the consumption of food.[98,99] Another desirable property of sunitinib as an anti-cancer agent is its ability to penetrate tissue and that it is highly protein bound.[98,102] Metabolism of sunitinib is mainly due to the activity of cytochrome P450 (CYP) 3A4 isoenzyme, which produces its primary active metabolite, SU1266 that is rendered inactive following further metabolism by CYP3A4.[102] Following metabolism, sunitinib is excreted from the body via renal and also hepatobiliary clearance pathways. Collecting of a ^{14}C-labelled drug found 61% excreted in the feces and 16% in the urine.[99,102] Renal elimination of sunitinib was not found to be different between patients with renal function ranging from normal to those requiring hemodialysis.[102] The use of combination therapy involving TKI's with other agents makes drug-drug interactions an important factor to consider. Some important drug interactions of sunitinib include the anti-fungal drug, ketoconazole, a CYP3A4 inhibitor, and rifampin, a commonly used antibiotic.[98,102] A 50% increase in sunitinib and its metabolite, SU12662, exposure resulted when concomitantly administered with ketoconazole. It has been proposed that the sunitinib dose has to be decreased to 66% of the recommended dose to account for this drug-drug interaction.[102] Rifampin, as well as phenytoin and ritonavir, induce an increase in the activity of CYP3A4, which has been shown to reduce combined systemic exposure to sunitinib by 50% prompting the adjustment of dose to 175% of recommended dose.[98,103] Other CYP3A4 inhibitors such as some macrolide antibiotics, anti-HIV agents, antidepressants, calcium channel blockers, some steroids and several herbal and dietary components may also play important roles in a potential sunitinib toxicity reaction and over-exposure.[103]

Motzer *et al.* conducted phase III trial comparing the treatment of ccRCC patients with sunitinib, and interferon-α.[104] They found that the sunitinib-treated group had a significantly longer progression-free survival and objective response rate, compared to the interferon-α treated group.[104] Dose-escalation, different treatment schedules, and novel combinations are still underway to improve the efficacy and reduce toxicities associated with sunitinib.[105]

1.5 Tumor Hypoxia and Activated Pathways

1.5.1 Development of Tumor Hypoxia

Tumor hypoxia was first investigated by Thomlinson and Gray in 1953. They found that large tumors have a necrotic core surrounded by a viable rim of tumor cells in close proximity to a blood vessel.[106] As tumors develop and grow, they require increasing amounts of nutrients, including oxygen and the tumor demand eventually exceeds the supply of the vasculature, naturally leading to hypoxic conditions with quiescence and necrosis. A large proportion of tumors with a volume greater than 1 mm^3 contain these hypoxic regions due to increasing diffusion distances from the oxygen-supplying vessels to the centre of the tumor, and also disordered structure of vessels due to irregular proliferation of cells.[107] Shannon *et al.* added that along with poor vessel support to the tumors, decreased oxygen carrying capacity due to both tumor-associated and treatment-induced anemia can contribute to tumor hypoxia.[107] It has been shown that tumors with necrotic areas had lower oxygen tension than the surrounding tissue and were found to be 150 μm from the nearest blood supply.[108] Based on the importance of hypoxia in the development of a more aggressive malignancy and its effects in reduced drug efficacy, several techniques have been used to measure intra-tumoral hypoxia including oxygen microelectrode polarography, magnetic resonance, optical and different nuclear imaging methods.[109-111] Currently, the “gold standard” for assessing tumor hypoxia is oxygen microelectrode polarography.[111]

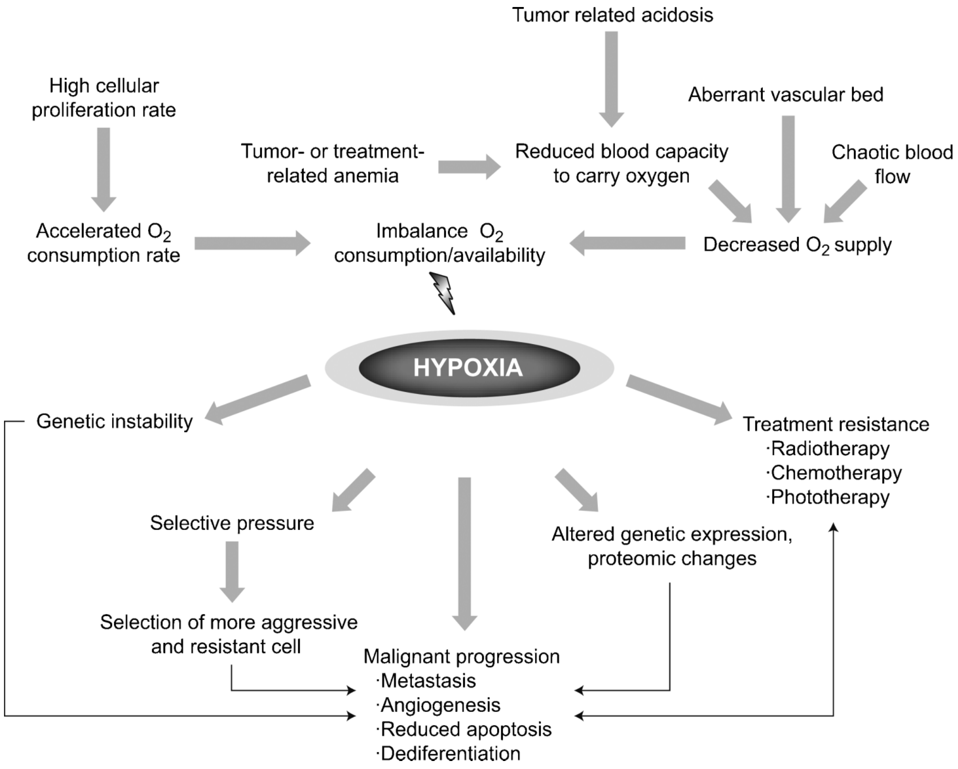

Figure 6: Hypoxia initiates several mechanisms for mitogenesis, migration and survival and is a key determinant of RCC phenotype[112]

Although it has been shown to accurately correlate with clinical outcomes, it is invasive, technically demanding, and is prone to sampling errors, prompting further investigation into other methods of assessing hypoxia in order to guide treatment and provide accurate prognosis to patients.[109] Non-invasive imaging techniques, however, are not without significant limitations as well.[110] There are also *ex vivo* approaches to determine tumor hypoxia utilizing the 2-nitroimidazole compound pimonidazole HCL, which forms intracellular adducts that can be readily detected by immunohistochemistry.

1.5.2 Cellular Response to Hypoxia

In response to hypoxia, several changes occur in the tumor cells including metabolic changes and development of new blood vessels to increase the supply of O_2 (nutrients) to the tumor (see Figure 6). As previously mentioned, these processes are mainly controlled by the HIF-1 transcription factor as the key regulator of these processes.[67,113] Under normoxic conditions, HIF-1α is deactivated by the ubiquitin-proteasome system, which is controlled by the VHL protein.[113] Under hypoxic conditions HIF-1α is not ubiquitinated (*vide infra*) and heterodimerizes with HIF-1β to form the functioning HIF-1 transcription factor.[113] Inactivating mutations of the tumor suppressor gene, VHL, lead to an activation of HIF, irrespective of the current microenvironmental conditions. Following the formation of the transcription factor, several adaptations to gene transcription occur that are important for cell survival. Some of these adaptations include the up-regulation of erythropoietin, glucose transporters, glycolytic pathway enzymes, VEGF, transferrin heme oxygenase and inducible nitric oxide synthetase.[113] By altering oxygen levels, Hatzikirou *et al.* were able to establish dominant tumor cell phenotypes corresponding to a ratio of proliferation/migration rates, specifically that the cells could be changed into the proliferation (high oxygen) and migration (low oxygen) phenotype by controlling the presence of oxygen.[114] The ability of the two subunits HIF-1α and HIF-1β, to dimerize is controlled by the degradation of HIF-1α, which occurs under normoxic conditions via the ubiquitin-proteasome system.[115] In turn, the VHL tumor suppressor gene codes for a protein that mediates the activity of the ubiquitin-proteasome system.[67] Specifically, a family of enzymes called prolyl hydroxylases adds hydroxyl (-OH) groups to proline residues on the HIF-1α subunit causing it to interact with an E3 ubiquitin ligase complex that targets HIF-1α for rapid degradation by the proteasome.[107,116] Degradation of HIF-1α ensures that the active transcription factor will not form, thereby preventing the transcription of hypoxia-survival associated genes. Vascular endothelial growth factor (VEGF), platelet derived growth factor (PDGF), transforming growth factor (TGF), epidermal growth factor (EGF) receptor, Glut-1 glucose transporter, and carbonic anhydrase IX, among others, are all gene products from HIF-1 transcription which act to increase angiogenesis and cell proliferation in order to improve tumor cell survival under hypoxic conditions.[116]

1.5.3 Clinical Significance of Tumor Hypoxia

In the clinic, hypoxia has been used as an indicator of patient responsiveness to chemotherapy, radiotherapy, photodynamic therapy, and plays an important role as a prognostic marker for patient outcome.[112] Hypoxia has been associated with heightened tumor aggressiveness and detrimental survival outcomes.[117] This can be attributed to increased motility, more angiogenesis (growth factors), evasion of apoptosis, increasing metastatic potential and a switch to anaerobic metabolism.[114] Being able to accurately measure tumor hypoxia could play an important role in predicting prognosis, determining therapeutic response to anti-angiogenic agents, and determining if it is targetable for adjuvant therapy.

1.6 Non-Invasive Diagnostic Imaging for RCC

1.6.1 Introduction

Several methods exist to detect and characterize cancerous masses including ultrasound (US), Computed tomography (CT), Magnetic Resonance Imaging (MRI), and Positron-Emission Tomography (PET). Imaging techniques aim to differentiate between benign and malignant tumors as well as provide information important for staging. In general, the first in line modality used is US due to its broad availability, low cost, and reduced exposure to radiation.[118] Furthermore, Doppler US has the ability to determine the vascularity of a lesion.[118] Currently, the most commonly used imaging modality to diagnose and stage RCC is CT. If surgical resection is not planned then immunohistochemical confirmation from biopsy specimen is also utilized.[119] CT potentially allows determination of the differentiation of RCC subtypes, and provides important structural information that can be used to guide the surgical resection of the mass.[118] A more structural specific imaging modality that is sometimes used to characterize more details of the renal mass is MRI due to its superior soft tissue contrast.[118] PET utilizing various radiotracer compounds labeled with short-lived positron emitting isotopes allows visualization of functional processes and metabolically active diseases *in vivo*.[118]

Recent advances in cross-sectional imaging modalities have improved physicians ability to detect renal tumors, allowing early detection and improved disease management with a better outcome regarding long-term survival of RCC.[11] Specifically for RCC, real-time and Doppler US are the most commonly used methods for initial diagnosis, but CT is being used as the golden standard for characterization, staging and surveillance of

RCC.[120] Functional imaging modalities including MRI and PET are currently emerging for patients with suspected metastatic disease. Application of PET may allow improvements in accuracy and specificity with the utilization of different PET radiotracers as well as the development of novel radiolabeled imaging probes for specific targets.[120] Furthermore, functional imaging is being evaluated in different preclinical and clinical studies for its use to evaluate patient response to targeted therapies, including anti-angiogenic agents such as sunitinib.[121]

1.6.2 Positron Emission Tomography

Positron emission tomography is a non-invasive imaging method used in nuclear medicine that allows radiotracer molecules labeled with a positron-emitting isotope such as ^{18}F, ^{11}C, ^{64}Cu, ^{68}Ga or ^{124}I to be detected and followed throughout the body. Positron decay and the subsequent emission of two gamma rays allow the localization and quantification of the radioactivity distribution. Different radiolabeled molecules can be used to monitor different physiological or pathophysiological processes. PET is utilized to detect disorders of the brain and cardiovascular system as well as in oncology.[122] In oncology, PET is used for the diagnosis, initial staging, and monitoring therapeutic response in several types of cancer including testicular, breast, prostate, brain, lung, colorectal, esophageal, head and neck, lymphoma and melanoma.[122] The first developed and still most commonly used PET radiotracer in oncology is [^{18}F]-fluoro-2-deoxy-2-glucose ([^{18}F]FDG), which exploits the metabolism of tumor cells to aid in the diagnosis and follow-up of patients with many types of cancer.[118] [^{18}F]FDG is used to measure glucose metabolism. Expression of GLUT transporters is up-regulated in most types of cancer leading to an increased glucose metabolism.[123] However, uptake of [^{18}F]FDG is not specific since it can also be elevated during inflammation or in benign lesions, leading to false positive interpretations and misidentification.[124] In contrast to normal cells that rely on oxidative phosphorylation to generate ATP to satisfy the cells energy demand, transformed cancer cells switch to aerobic glycolysis. This process has been termed as the Warburg effect.[125] There can be significant heterogeneity of [^{18}F]FDG uptake in RCC. However, RCC tumors are usually found to have similar uptake intensity to the surrounding renal parenchyma. Furthermore, the renal clearance of radiolabeled tracers makes detection of localized kidney tumors even more difficult. In recent clinical studies, [^{18}F]FDG-PET was evaluated for its use in the clinic in detecting metastatic RCC and also as a biomarker for patient response to targeted cancer therapy.[118] Besides glucose metabolism, cell proliferation, tumor microenvironment and many other specific targets as well as physiological processes can be observed with PET.

1.6.3 Imaging Tumor Hypoxia

Hypoxia is one characteristic parameter of a tumor's microenvironment. As detailed above, tumor hypoxia results from rapid proliferation of cancer cells, along with pathological angiogenesis. Hypoxia is found in many tumor types, and plays an important role in gene transcription, disease progression, and treatment resistance, which makes it an attractive property to measure. Besides utilization of oxygen electrodes, other techniques including histomorphometric analysis, DNA strand break analysis (comet assay), and various hypoxia markers that are detected by MRI and immunohistochemistry, and radiolabeled molecules for methods such as single photon emission computed tomography (SPECT), PET, autoradiography and gamma scintillation counting can be used to determine tumor oxygenation levels.[126] Over the past few decades, several specific hypoxia tracers have been developed and investigated. The 2-nitroimidazoles were among the first compound class to be developed and they are still the most commonly used molecules for specific binding and trapping in hypoxic cells. The mechanism of reduction and intracellular retention of 2-nitroimidazoles involves the formation of a radical anion, which reacts preferentially with O_2 if it is present to return the tracer into its original form. Under hypoxic conditions, when O_2 is not present, it accepts another electron to produce an intermediates that is sequentially reduced to highly efficient alkylating agents with hydroxylamine functional groups, resulting in the intracellular retention of labeled tracer via formation of covalent bonds to intracellular macromolecules.[127,128] Early analysis of tumor hypoxia with ^{14}C-labeled misonidazole revealed a selective binding to hypoxic cells within a tumor.[129] Based on their lipophilicity 2-nitroimidazoles enter a cell via passive diffusion before being reduced under hypoxic conditions and subsequentially trapped in the cells. 2-Nitroimidazole derivatives were initially developed as low-toxicity oxygen mimetic radiosensitizers for radiotherapy of hypoxic tumors.[130] Depending on the radioisotope (iodine-123, -124, -131 or fluorine-18), 2-nitroimidazoles can be used for imaging tumor hypoxia as SPECT or PET agents.[131,132] To date the misonidazole (MISO) derivative [^{18}F]-fluoromisonidazole ([^{18}F]FMISO), is still the most widely used PET agent for hypoxia imaging.[133] Fluoroarabinofuranosyl-2-nitromidazole ([^{18}F]FAZA) was exploited to improve image contrast by increasing the rate of clearance from blood and from non-target tissue.[134] [^{18}F]FAZA was developed from iodoarabinofuranosyl-2-nitromidazole

([^{123}I]IAZA), which is an effective SPECT agent.[135,136] [^{18}F]FAZA is a more hydrophilic 2-nitroimidazole than [^{18}F]FMISO and 2-(2-nitro-1*H*-imidazol-1-yl)-*N*-(2,2,3,3,3-[^{18}F]pentafluoropropyl)-acetamide ([^{18}F]EF5), the latter one being the most lipophilic molecule among those three 2-nitroimidazoles.[128]

Based on the different lipophilicity of the 2-nitroimidazoles they differ in their biodistribution and their ability to cross the blood brain barrier. [^{18}F]FAZA being the most hydrophilic molecule compared to [^{18}F]FMISO and [^{18}F]EF5 would only cross a damaged blood brain barrier. It also penetrates less into soft tissue, which may be of an advantage in achieving a faster target uptake-to-background ratio. In addition to [^{18}F]FAZA, [^{18}F]FMISO and [^{18}F]EF5 several other 2-nitroimidazoles have been synthetized and evaluated for their potential use as PET radiotracers (see Figure 7).[137]

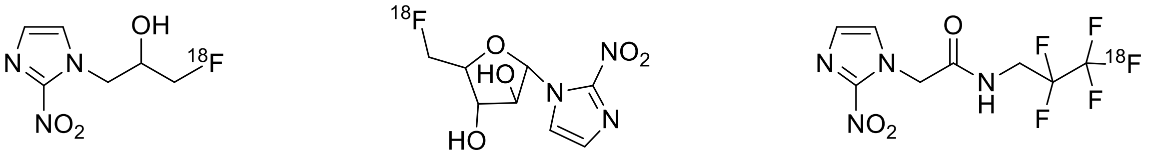

[^{18}F]FMISO [^{18}F]FAZA [^{18}F]EF5

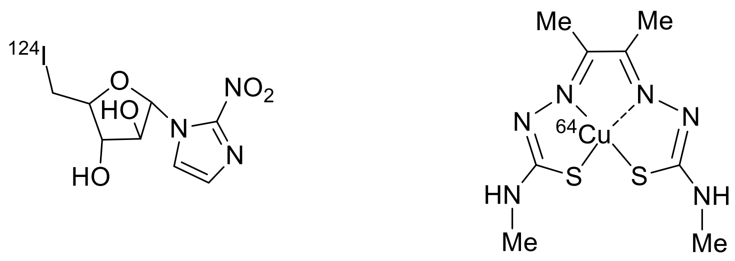

[^{124}I]IAZA [^{64}Cu]ATSM

Figure 7: Hypoxia PET radiotracer - most commonly used ^{18}F and ^{124}I-labeled 2-nitroimidazoles and ^{64}Cu-labeled ATSM.

Beside the fluoro- and iodo-labeled 2-nitroimidazoles, copper-labeled compounds also have been developed for imaging tumor hypoxia.[128] Copper has several different positron (β^+) emitting isotopes (^{60}Cu, ^{61}Cu, ^{62}Cu and ^{64}Cu) with half-lives ranging from 9.8 min to 12.7 h. Among them ^{60}Cu and ^{64}Cu are the two most commonly used copper isotopes for PET imaging applications.[138] The neutral, lipophilic copper (II) complex of diacetyl-2,3-bis(N4-methyl-3-thiosemicarbazone), commonly referred to as Cu-ATSM, shows selective hypoxic uptake.[139] Cu(II)-ATSM freely diffuses in and out of cells. Cu(II)-ATSM is reduced to $[\text{Cu(I)-ATSM}]^-$, and in the presence of O_2 it can be re-oxygenated to the parent compound again, subsequently leaving the cells. Under hypoxic conditions $[\text{Cu(I)-ATSM}]^-$ is trapped and may dissociate and transfer the radiocopper to other intracellular macromolecules.[139]

Over the past two decades, numerous clinical and experimental studies have been performed to determine the hypoxic status of solid tumors before, during and after therapy utilizing different radiotracers.[140-142] To date, an important goal still remains in proving that determination of tumor hypoxia can be clinically utilized as a predictive marker for a better therapy outcome. Thus, molecular imaging of tumor hypoxia would potentially have two clinically important roles: (i) selecting patients that may respond better to treatment design to overcome the poor prognosis of tumor hypoxia levels and (ii) serial imaging of tumor hypoxia to determine the treatment effects by visualizing a reduced hypoxic status of a solid tumor.[128]

Originally, emphasis was placed on measuring tumor hypoxia when it was first discovered that it correlated with a lack of tumor response to radiation therapy.[128] Furthermore, since hypoxia is common in most solid tumors, significant efforts have been made to elucidate hypoxia as a potential therapeutic target. Most notably, research in this field has explored the use of tirapazamine, a hypoxia-activated cytotoxin.[143] An increase in hypoxia may present a novel target to provide a therapeutic advantage using hypoxia-activated cytotoxins. In addition to being a potential target for therapy, hypoxia markers can be used to monitor patient response to targeted therapy. Conversely, tumor hypoxia has been shown to lead to more metastatic and resistant cancers (*vide supra*) partly based on drug delivery, quiescence, and lack of oxygen to fix radiation-induced radicals. Based on this a reduction of hypoxia should correlate with a decrease of metastases occurrence, along with enhanced tumor response to therapy. High [^{18}F]FAZA uptake has been shown to be an independent adverse prognostic factor for tumor progression and can also be used to identify patients who may experience increased resistance to particular therapies.[144] Monitoring tumor oxygenation during and after treatment should be able to indicate therapeutic response and clinical outcomes in a patient, and guide personalized treatment options.

1.7 Rationale and Hypothesis

Based on the touted therapeutic mechanism of action of sunitinib, the current study focuses on the use of positron emission tomography to detect changes in the renal cell carcinoma microenvironment. Currently, there is controversy surrounding the effect of sunitinib and other anti-angiogenic agents on tumor hypoxia.[5,145-148] Some studies have found that normalization of vasculature results, including an attenuation of hyperpermeability, increased pericyte coverage, a more normal basement membrane, along with a decrease in interstitial fluid pressure and tumor hypoxia.[149] Other studies suggest that a decrease in vascular density results in the induction of greater tumor hypoxia.[5] Based on the above information, we hypothesized that imaging with the hypoxia PET tracer, [^{18}F]FAZA, at different time points throughout short-term and long-term sunitinib therapy could further elucidate the understanding of the relationship between anti-angiogenic therapy and the tumor microenvironment.

Chapter 2: Materials and Methods

2.1 Animal Models for RCC

All animal experiments reported here were carried out in accordance with the guidelines of the Canadian Council on Animal Care and approved by the local Institutional Animal Care Committee of the Cross Cancer Institute (University of Alberta, Edmonton, Canada). Female athymic BALB/c nu/nu mice weighing 17-20 g were used for tumor implantation and randomly assigned to the experimental groups. Animals were purchased from Charles River Laboratories (Quebec, Canada). Sterile technique was used for all procedures including catheterization of the animals.

2.1.1 Subcutaneous Flank Caki-1 Model

Caki-1 is a human epithelial kidney clear cell carcinoma cell line derived from a metastatic site. Previously frozen tumor fragments (~1.5 mm^3) from tumors formed from subcutaneous injection of a Caki-1 cell suspension (1x10^6 cells) in a separate animal, were implanted into the left and right flank of athymic BALB/c nu/nu mice. For this procedure mice were placed under isoflurane anesthesia. The skin area was prepared using an iodine solution and rinsed with isopropanol. A small incision of ~2-3 mm in length was made, and the Caki-1 tumor fragment was placed inside the formed subcutaneous pocket. The incision was closed with 4-0 silk sutures and again rinsed with isopropanol. Tumor growth was monitored daily. After 5 days, tumors began to grow and when they reached an appropriate size of 5-10 mm in diameter were used for all following experiments.

2.1.2 Orthotopic Caki-1 Model

Female athymic BALB/c nu/nu mice were also used to establish the orthotopic (renal subcapsule) RCC model. A tumor fragment (1.5 mm^3) from a subcutaneous Caki-1 tumor also grown in a different animal was implanted into the subcapsule of the right kidney. The surface of the right kidney was exposed from an 8 mm flank incision with gentle abdominal pressure. A small puncture near the lower pole was made with the tip of a sharp 18 gauge beveled needle and the tumor fragment was inserted with microsurgery forceps. After hemostasis was obtained with gentle pressure, the kidney was then gently pushed back to its normal position and the incision was closed with a simple 4-0 suture and tumor growth was allowed for 3-4 weeks (based on prior studies) before PET imaging.

2.2 Positron Emission Tomography and Biodistribution

Positron emission tomography (PET) experiments were performed on BALB/c nu/nu mice bearing subcutaneous or orthotopic Caki-1. Non-fasted animals were anesthetized using inhalation of isoflurane in 40% oxygen/60% nitrogen (gas flow, 1L/min), and body temperature maintained constant at 34-37 °C for the entire experiment using a standard small animal heating pad. For PET imaging, a catheter was placed into the tail vein of the mouse. Under anesthesia, mice were placed in the prone position with their medial axis parallel to the axial axis of the scanner and their thorax, abdomen, hind legs in the centre of the field of view of the microPET® R4 scanner (Siemens Preclinical Solutions, Knoxville, TN, USA; see Figure 8). A transmission scan for attenuation correction was not acquired.

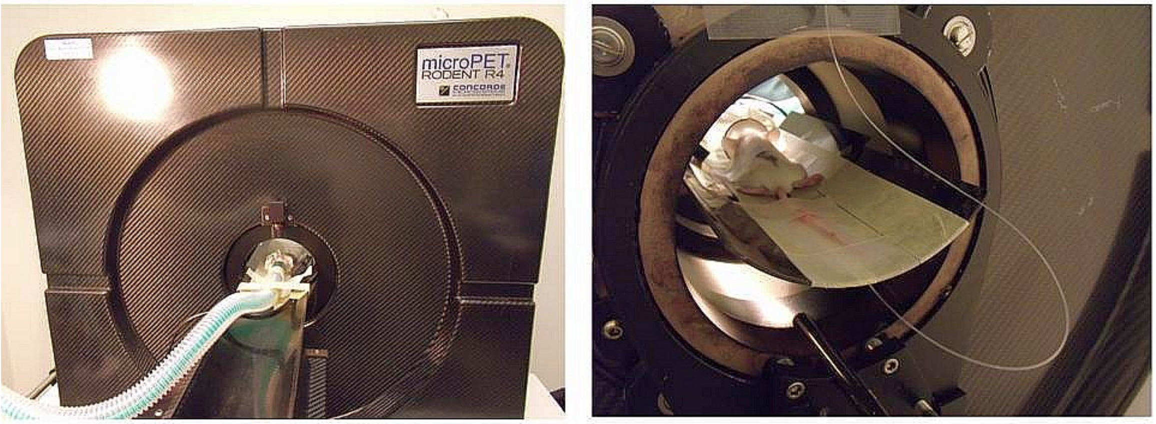

Figure 8: PET experimental setup: A mouse in a microPET R4 scanner (Siemens Preclinical Solutions; ©Division of Oncological Imaging, University of Alberta)

Prior to injection, the amount of radioactivity present in the 0.5 mL syringe was determined using a dose calibrator (Atomlab 300, Biodex Medical Systems, Shirley, NY, USA). The dose calibrator was cross calibrated with the scanner. For the different experimental protocols, an emission scan of either 180 min (dynamic experiments) or 10 min (static scans) PET acquisition was initiated. After a 15 s delay, 4-5 MBq of the radiotracer of interest ([^{18}F]FDG or [^{18}F]FAZA) in 100-150 µL saline was injected intravenously through the catheter into the tail vein. The injection solution of [^{18}F]FAZA contained up to 8% EtOH. Both radiotracers were provided by the Edmonton PET Center at the Cross Cancer Institute (University of Alberta, Edmonton, Canada). Depending on the experimental setup, data acquisition continued for either 180 min or 10 min in 3D list mode. The dynamic list mode data were sorted into sinograms with 59 time frames (10x2, 8x5, 6x10, 6x20, 8x60, 10x120, 10x300 s). The frames were reconstructed using Ordered Subset Expectation Maximization (OSEM) or maximum a posteriori (MAP) reconstruction modes. The pixel size was 0.085x0.085x0.12 cm, and the resolution in the center field of view was 1.8 mm. Correction for partial volume effects was not performed. The image files were further processed using the ROVER v2.0.21 software (ABX GmbH, Radeberg, Germany). Masks defining 3D regions of interest (ROI) were set and the ROIs were defined by thresholding. Time-activity curves (TAC) were generated from each ROI for subsequent data analysis. Mean standardized uptake values [SUV_{mean} = (activity/mL tissue)/(injected activity/body weight), mL/g] were calculated for each ROI.

After a PET scan was finished, mice were immediately sacrificed by cervical dislocation and muscle tissue, liver, left and right kidney, and the left and right tumor were collected in scintillation vials, weighed and counted using a Wizard-3 1480 automatic gamma counter (Perkin Elmer Life Sciences, Woodbridge, ON, Canada). Before counting and after weighing the tumor tissue was covered with formalin to save it for further immunohistochemical analysis. Biodistribution experimental results were analyzed as percentage of injected dose per gram of tissue (%ID/g) or as standardized uptake values (SUV).

2.2.1 Animal Tumor Model Characterization

Mice bearing both a left and right subcutaneous Caki-1 flank tumor, or one orthotopic caki-1 tumor in the right kidney, were injected with [^{18}F]FDG or [^{18}F]FAZA. Dynamic PET acquisition was performed for 180 min. These experiments were carried out to analyze the pharmacokinetic uptake profile of the radiotracers in the Caki-1 RCC tumor model.

2.2.2 Effect of the TKI Inhibitor Sunitinib

Following characterization of the Caki-1 RCC tumor model *in vivo*, a new set of mice bearing two subcutaneous Caki-1 tumors were established. Once tumors reached an appropriate size (10-15 mm in diameter) for PET imaging, the drug treatment with sunitinib was initiated. Pure sunitinib malate was a gift from Pfizer Canada (Kirkland, Quebec, Canada). Animals were randomly assigned into two different treatment groups: A) receiving an intraperitoneal injection of 40 mg/kg/day of sunitinib malate in 1%DMSO in saline for 5 days, and B) a control group receiving vehicle injections (1%DMSO in saline). Again, 3 h dynamic PET acquisitions were performed in order to study changes in the radiotracer's tumor uptake profile under therapy with sunitinib. Following the PET scans, mice were euthanized by cervical dislocation and organs of interest were harvested for *ex vivo* biodistribution analysis.

2.2.3 Long term therapy with sunitinib plus treatment cessation

Long term therapy was done in a similar way as the analysis of the short term therapy effect of sunitinib (*vide supra*). Thirty mice were implanted with Caki-1 tumor chunks grown in a donor animal. Each mouse received two tumor implants one on the left and one on the right upper flank. After 10 days of growing, tumor-bearing mice were randomly assigned into two groups: A) receiving an intraperitoneal injection of 40 mg/kg/day of sunitinib malate in 1% DMSO in saline for up to 15 (5 days on, 2 days off) days following treatment interruption for another 12 days, and B) a control group receiving vehicle injections (1%DMSO in saline) over the same period of time as the sunitinib treatment was done following interruption without any vehicle injection for the same time as the treatment with sunitinib was stopped in group A. After 4, 9 and 13 days of sunitinib treatment as well as 15 days of treatment plus 12 days therapy interruption, selected mice from both groups were injected with [^{18}F]FAZA and analyzed with static PET measurements as well as *ex vivo* biodistribution 3 h post injection. Mice were put under isoflurane anesthesia and PET data was acquired for 10 min. After the PET scan was finished, mice were immediately sacrificed by cervical dislocation and muscle tissue, liver, left and right kidney, and the left and right tumor were collected in scintillation vials and counted in the Wizard gamma counter. Before counting and after weighing the tumor tissue was covered with formalin to save it for further immunohistochemical analysis.

2.2.4 Data Analysis and Statistics

All data are expressed as means ± S.E.M. from n number of tumors out of x investigated animals (n/x). All time activity curves and bar graphs were constructed using GraphPad Prism® 4.0 (GraphPad Software). Where applicable, statistical differences were tested by Student's t-test and were considered significant for $p < 0.05$.

2.3 Comparative Immunohistochemistry

Following euthanization and harvesting of the organs and tissue, tumor tissue samples were submitted to histology for formalin-fixed paraffin embedded tissue slides. After the samples were fixed, tissues were embedded in wax and sectioned at 3 microns and transferred to glass slides for storage. Prior to immunohistochemical staining, slides were placed in a rack and incubated at 60 °C for 1 h. Following removal of the wax, tissue was rehydrated with a sequence of baths starting with xylene, then 100% ethanol, 80% ethanol, 50% ethanol, and then 2 minutes in H_20/0.2% Brij-35 (a nonionic detergent for use in various protein methods), and then 2 minutes in PBS/0.2 Brij-35. Heat-induced epitope retrieval method was used. Following hydration, samples were placed in a pressure-cooker with 700 mL of 10 mM citrate buffer - 0.05% - tween - 20 at a pH of 6.0. The pressure-cooker was sealed and placed in the microwave on high for 20 min. To ensure a proper seal, at 18 min, a hissing sound from the microwave was observed. After 20 min, the pressure-cooker was removed and left on the bench to cool for 25 min. After that the samples were rinsed under with water for 20 min and placed in double de-ionized H_20 bath.

2.4.1 Pimonidazole HCl

Three hours prior to sacrificing the animal, pimonidazole HCl compound (Hypoxyprobe, Inc., Burlington, MA, USA) was injected via mouse tail vein at a dose of 60 mg/kg. After the antigen retrieval step, the slides were placed in a glycine block (500 mM in PBS/0.02% Brij-35 97 (polyethylene 10 oleoyl ether) for 30 min at room temperature without letting the tissue dry out. Using a hydrophobic peroxidase-anti-peroxidase (PAP) pen, tissue was marked prior to the addition of the other reagents. Next, peroxidase block (Dako, Denmark) was added to the tissues for 10 min. Following the block of peroxidase activity, the primary anti-body was added (1/1000 dilution) and incubated for 1 h at room temperature. The slides were then rinsed and dipped in PBS/0.02% Brij-35 solution for 5 min. Then one drop of Dako Cyomation Envision-horseradish peroxidase (HRP) was added and allowed to incubate for another hour. Again, the samples were rinsed in PBS/0.02% Brij-35. Fifty uL of chromagen (1 drop of DAB + 1 mL of chromagen substrate) was added to each slide and the reaction was allowed to take place over 10 min. Placing the slides in double de-ionized H_2O stopped the reaction. A few drops of copper sulphate (1%) were added on each slide and incubated for 5 min. The slides were then dipped in hematoxylin for 5 s and rinsed under hot water until they were clear. The tissues were then dehydrated using the reverse sequence as described above and cover slips were added on top of the slides.

2.4.2 CD-31 Platelet Endothelial Cell Adhesion Molecule (PECAM) Labeling

Following rehydration and antigen retrieval steps, the slides were soaked in 1%Triton-X/Tris Buffer Solution (TBS) for 30 min. They were then placed in 1% Fish Skin Gelatin/0.1%Triton-X/TBS for 1 h. After this blocking step, the primary CD-31 antibody (Rabbit polyclonal anti-mouse CD-31, Santa Cruz Clone:M20) diluted to 1/2500 in antibody diluent was applied for 20 min. The slides were then washed twice for 10 min each in 500 mM total salt-0.05% Triton-X/TBS. Peroxidase block was then added for additional 5 min and then washed with 0.05%TBST for another 5 min, and repeated three times. A Tyramide Signal Amplification (TSA) reagent (1/50 dilution in amplification diluent, Perkin Elmer TSA kit) was added for 5 min. After that the slides were washed in 0.05% TBST/5 min three times. SA-HRP/1%Fish Skin Gelatin/0.1%Triton-X/TBS diluted 1/100 was added for 30 min and the slides were washed three times again with 0.05%TBST for 5 min. The slides were then developed with chromogen (one drop of DAB + 1 mL of chromogen substrate from DAKO) for 5 min. The slides were then rinsed with water and dipped in hematoxylin for 1 s and rinsed under hot water until it they were clear. Color was enhanced by dipping slides in lithium carbonate and rinsed again with hot water. The slides were then dehydrated before mounting the cover slip.

2.4.3 Data Analysis and Statistics

All data are expressed as percent antibody binding and as means ± S.E.M. from n investigated tissue slices. The bar graphs were constructed using GraphPad Prism® 4.0 (GraphPad Software). Where applicable, statistical difference was tested by Student's t-test and were considered significant for $p < 0.05$.

2.5 *In Vitro* Hypoxic Cell Labeling Experiments

2.5.1 Cell Culture Conditions

For these experiments the human renal cell carcinoma cell lines Caki-1 (ATCC) and the human mammary carcinoma cell line MCF-7 (a gift from Dr. David Murray, Cross Cancer Institute, University of Alberta) were used. The cell lines were cultured at 37 °C and 5% CO_2 (standard conditions) in F-12/DMEM medium supplemented with 10% fetal bovine serum, 2 mM glutamine, 1% penicillin/streptomycin, 10 mM HEPES, 1 mM sodium pyruvate, and 1% non-essential amino acids. Cells were passaged every 2-3 days until the final experimental setup was prepared.

2.5.2 Experimental Set-up

Using glass cell culture dishes with a diameter of 55 mm, cells were plated at a density of ~500,000 cells per plate and incubated for 48 h 37°and 5% CO_2. Following that time, half of the plates were taken for culturing the cells under hypoxic conditions over the next 24 h, the others were kept under normal cell culture conditions. Hypoxic cell culture conditions were achieved using a special sealed chamber device (Figure 9), in which O_2 can be nearly entirely replaced with N_2.

Figure 9: *In vitro* cell experimental setup: Air tight culture chambers attached to degassing system (vacuum and nitrogen gas supply) to induce hypoxic conditions in these chambers.

The glass cell culture dishes were placed into the chambers and the lid was closed and sealed. Then the chambers were connected to a degassing/gassing system. The degassing line was first evacuated using a vacuum pump. Pressure was reduced to the lowest value possible, and the vacuum was then shut off. Subsequently, the system was filled with N_2 and 5% CO_2. This step was repeated three times to ensure a low residue O_2 level only. Once the line was cleared, the cell-containing sealed chambers were attached to the system. The entire system was then tested for leaks by evacuating the chambers using the vacuum pump (no further than negative 600 mm Hg, to prevent boiling of media). The valves were then closed and the pressure gauge was observed for any differences over a period of 2 min. In order to reduce the canister to anoxia, the chambers were evacuated to 600 mm Hg and replaced with N_2. After 10 s, this step was repeated a total of four times. The chamber was then degassed to 600 mm Hg and replaced with N_2. The valve on the canister was then closed and left for 8 min to allow gas exchange between the liquid and the gas phases. This step was repeated a total of 4 times. Next, the chambers were degassed and replaced with N_2 and left for 10 s, repeating this step again for four times. The chambers were then transported to an incubator where they would remain together with the cells under normal culture conditions for 24 h prior to the cell uptake experiment. Following 24 h of incubation under normoxic and hypoxic conditions, cells were removed from the incubator and two samples from each condition were placed aside for protein quantification (bicinchoninic acid (BCA) assay) and background activity measurements. Media was aspirated and 2 mL of Krebs Ringer buffer (115 mM NaCl, 5.9 mM KCl, 1.2 mM $MgCl_2$, 1.2 mM NaH_2PO_4, 1.2 mM Na_2SO_4, 2.5 mM $CaCl_2$, 25 mM $NaHCO_3$, 5mM glucose at pH of 7.4) at room temperature were added to all plates. Radiotracer solution was then prepared by adding 30-40 MBq of $[^{18}F]$FAZA (H_2O/8 % ethanol) into 35 mL of Krebs Ringer buffer. To each plate 1 mL of the radiotracercontaining buffer was added. 90 μL of 10^{-4} M sunitinib maleate (in DMSO) was added to selected plates at this step to test for potential effects of the TK inhibitor on tracer uptake and retention. The plates were then placed back either to the incubator (normoxic conditions) or to the canister-chambers and degassed again using the same procedure as described above to reach hypoxic conditions in those chambers. After gas exchange in the chambers the sealed containers were also placed into an incubator. All cells were allowed to incubate for 4 hours with [^{18}F]FAZA added to each cell culture dish. Following this incubation, all plates were removed from the incubator, aspirated and washed 3 times with ice cold Krebs Ringer solution. Three mL of trichloroacetic acid (TCA) were added to each plate to allow cells to lysate for 1 h. Three mL of trypsin was added to the each of the protein sample plates that were set aside at the beginning and allowed to incubate for 10 min. The cells were then collected, centrifuged, and the pellet was frozen for the BCA assay for protein quantification the next day. Protein levels were quantified using the BCA protein assay kit (Pierce, Rockford, IL, U.S.A.) according to the manufacturer's recommendations and bovine serum albumin was used as the protein standard. Following the 1 h incubation of TCA in all other experimental plates, the supernatants were collected and placed into scintillation vials to be counted using the Wizard gamma counter (Wallac 1480 Wizard-3, Perkin-Elmer, Woodbridge, Ontario, Canada) in order to determine radioactivity uptake levels in the cells.

2.5.3 Data Analysis and Statistics

Cell uptake levels were normalized to percent of the total added amount of radioactivity corresponding to injected dose (%ID) per mg protein. All data are expressed as means ± S.E.M. from n cell uptake experiments. All bar graphs were constructed using GraphPad Prism® 4.0 (GraphPad Software, San Diego, CA, U.S.A.). Where applicable, statistical differences were tested by Student's t-test and were considered significant for $p < 0.05$.

Chapter 3: Results

3.1 Characterization of the *In Vivo* Model

3.1.1 Tumor Growth Characteristics

In order to characterize the model, the tumor growth characteristics of the subcutaneous Caki-1 RCC tumors were first monitored by measuring tumor dimensions every 3-4 days. Using three dimensions, the ellipsoid volume formula, π(LxWxH)/6, was used to determine the volume of the tumors. Tumor volume was plotted over time to visualize the rate of tumor growth. Figure 10 A) shows the tumor growth in the first set of 8 BALB/c nu/nu mice bearing two subcutaneous Caki-1 tumors each on their left and right upper flank. Figure 10 B) depicts another set of 8 mice which were used for the longer sunitinib therapy study (see 3.2.2.). In these mice the tumor growth was observed for up to 40 days after tumor implantation.

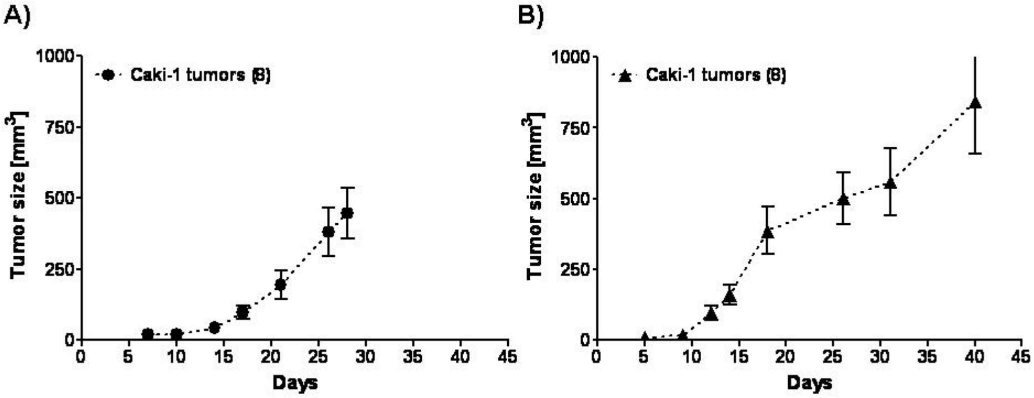

Figure 10: Tumor growth characteristics in Caki-1 bearing BALB/c nu/nu mice. A) Tumor growth was observed in 8 mice for 28 days; B) the growth was observed for up to 40 days after implantation.

At the end of the first set of growing Caki-1 tumors, a tumor volume of 447 ± 90 mm^3 (n=8) was measured after 28 days. During the second set of experiments a similar tumor size of 501 ± 91 mm^3 (n=8) was observed after 26 days of growth leading to a final size of 842 ± 184 mm^3 (n=8) at the end of the experiment at day 40. Both studies revealed a comparable tumor growth rate after the implantation of Caki-1 tumor pieces grown for 3-4 weeks in a donor BALB/c nu/nu mouse after the injection of 10^6 cells, respectively.

3.1.2 Uptake of [^{18}F]FDG and [^{18}F]FAZA

Prior to determining the effects of a sunitinib therapy on Caki-1 tumor's oxygenation, the uptake levels of the PET radiotracers [^{18}F]FDG (measuring tumor metabolism) and [^{18}F]FAZA (analyzing tumor hypoxia) were determined in BALB/c nu/nu mice bearing two Caki-1 tumors on each upper flank. For both radiotracers three hours dynamic PET scans were performed in order to analyze the tumor uptake profiles over time. Figure 11 shows representative images at various time points for the uptake of [^{18}F]FDG with a visible tumor uptake after 5 min (perfusion phase) and slightly increasing over the time course of 3 h (metabolic phase). From the dynamic PET experiments, time-activity curves (TACs) were generated by analyzing radioactivity uptake levels over time in a defined region of interest (ROI) over the tumor and muscle tissue (Figure 12). For [^{18}F]FDG a mean standardized uptake value (SUV_{mean}) of 0.60±0.02 (n=6/3) was determined after 3 h p.i..

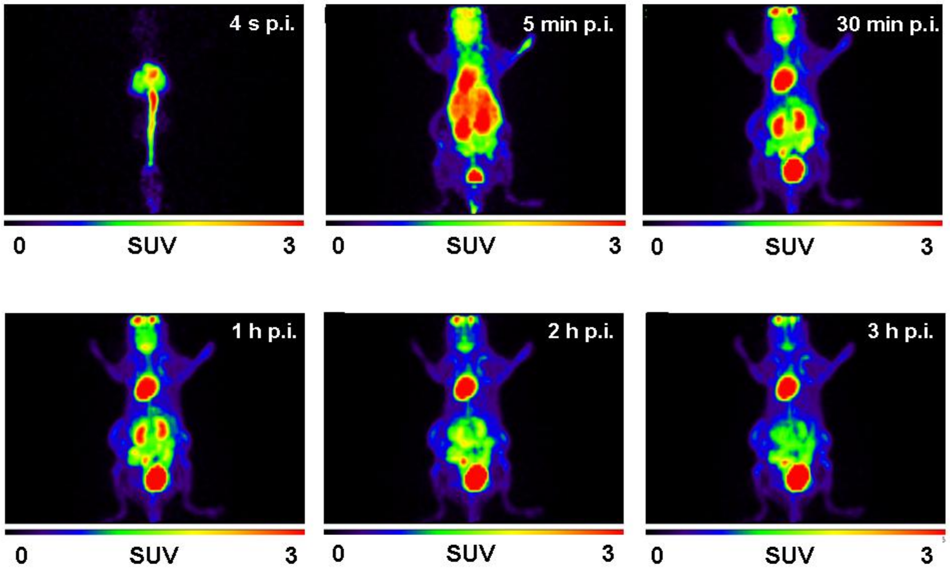

Figure 11: PET images of the uptake of [^{18}F]FDG into a BALB/c nu/nu mouse bearing 2 subcutaneous Caki-1 tumors. Images are shown as maximum intensity projections (MIP) at 4 s, 5 and 30 min, 1, 2 and 3 h p.i. of 6.56 MBq of the radiotracer.

From the TAC, it is visible that the uptake of [^{18}F]FDG only slightly increased over time (SUV$_{mean}$ 0.56±0.02; n=6/3 after 1 h p.i.).

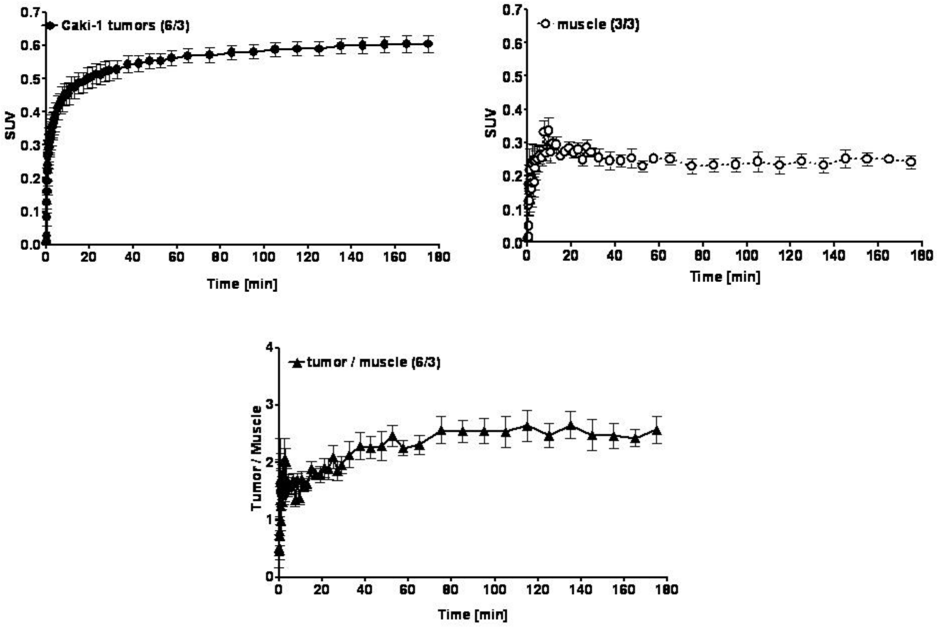

Figure 12: Time-activity curves (TACs) for the uptake of [^{18}F]FDG into Caki-1 tumors (top left) and muscle tissue of BALB/c nu/nu mice (top right) as well as the calculated tumor/muscle ratios (bottom).

In these mice [^{18}F]FDG had a low uptake level in muscle tissue (SUV$_{mean}$ 0.25±0.01; n=3 after 1 h p.i.), which was not washed out over time (SUV$_{mean}$ 0.24±0.02; n=3 after 3 h p.i.), leading to an only slightly increasing tumor/muscle ratio over the first 60 min, which was found to plateau over the next two hours (Figure 12). Figure 13 shows representative images for the uptake of [^{18}F]FAZA. The uptake into subcutaneous Caki-1 tumors was visible over time, while the radiotracer was clearing from the rest of the body.

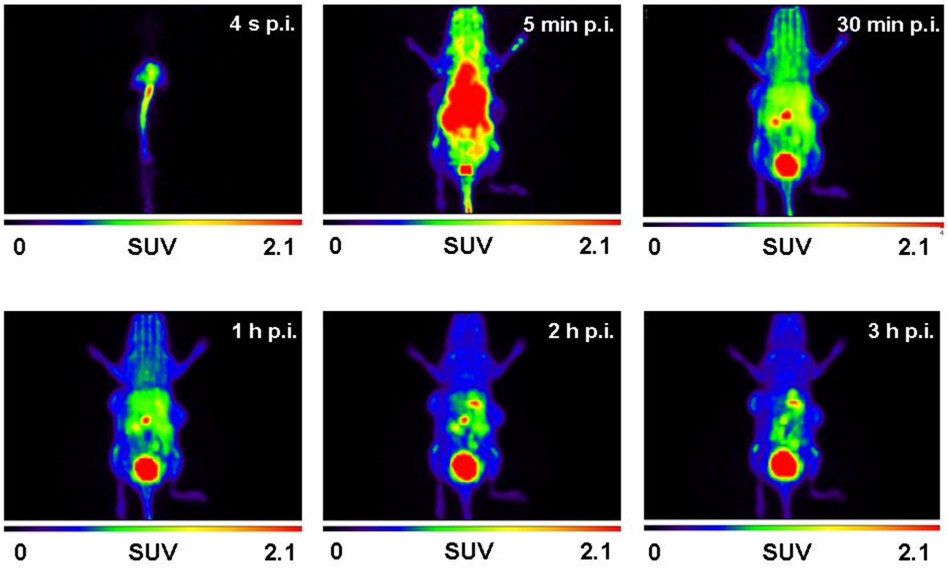

Figure 13. PET images of the uptake of [^{18}F]FAZA into a BALB/c nu/nu mouse bearing 2 subcutaneous Caki-1 tumors. Images are shown as maximum intensity projections (MIP) at 4 s, 5 and 30 min, 1, 2 and 3 h p.i. of 7.83 MBq of the radiotracer.

Analysis of the TACs revealed a rapid uptake of [^{18}F]FAZA into the tumor tissue and resulted in a SUV$_{mean}$ of 0.35±0.03; n=6/3 after 1 h p.i. and an almost unchanged SUV$_{mean}$ of 0.32±0.02; n=6/3 after 3 h p.i., respectively (Figure 14). Compared to the absolute tumor uptake of [^{18}F]FDG, the absolute uptake level for [^{18}F]FAZA was lower. Based on a similar radiotracer uptake into the muscle tissue (SUV$_{mean, 1h}$ of 0.33±0.06;

n=6/3) the overall [^{18}F]FAZA uptake into the Caki-1 tumor cells was very low. However, the radiotracer was clearing from the muscle tissue (SUV$_{\text{mean, 3h}}$ 0.23±0.04; n=6/3) and therefore the tumor/muscle ratio increased over time leading to a value of 1.56±0.12 (n=4) after 3 h p.i. (Figure 14).

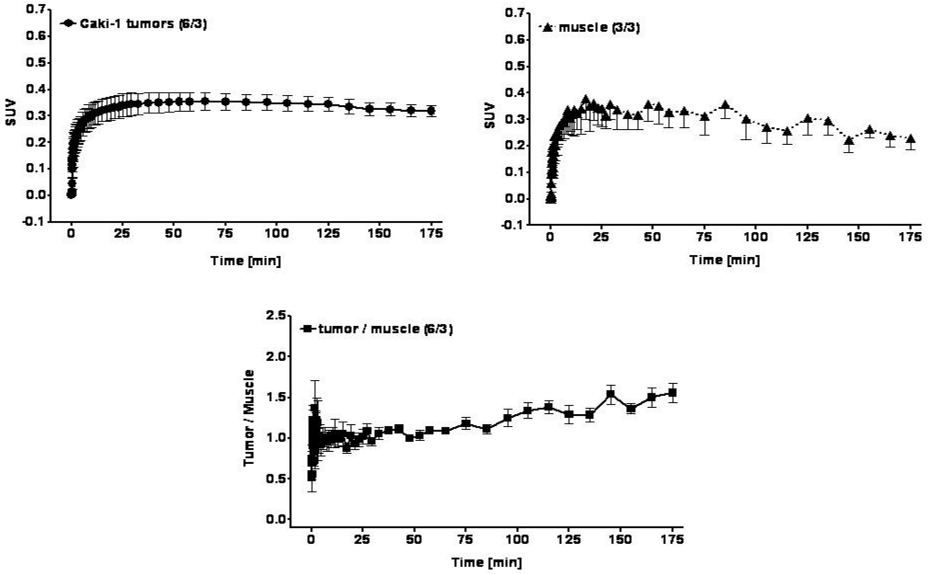

Figure 14: Time-activity curves (TACs) for the uptake of [^{18}F]FAZA into Caki-1 tumors (top left) and muscle tissue of BALB/c nu/nu mice (top right) as well as the calculated tumor/muscle ratios (bottom).

In addition to subcutaneous Caki-1 tumors, an orthotopic RCC model was analyzed (tumor grown in the right kidney capsule). Both PET radiotracers, [^{18}F]FDG and [^{18}F]FAZA, were investigated. However, based on their Caki-1 tumor uptake and clearance pattern, the orthotopic tumors could not be detected and delineated in these mice with PET alone (Figure 15).

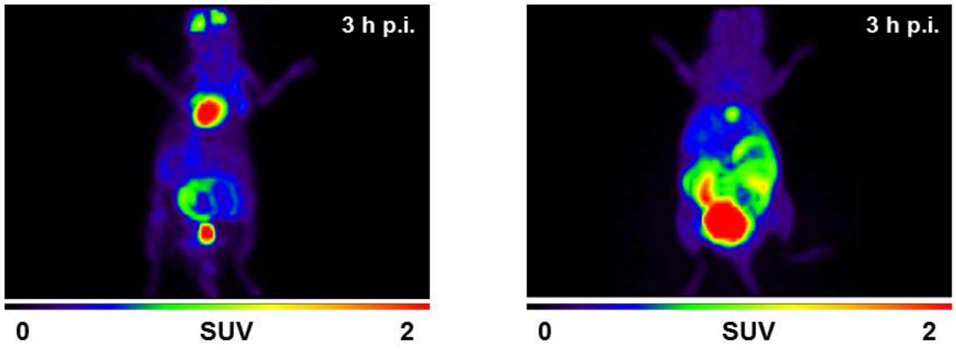

Figure 15: [^{18}F]FDG (left) and [^{18}F]FAZA (right) at 3 h p.i. in BALB/c nu/nu mouse bearing one orthotopic Caki-1 tumor (right kidney capsule). Images are shown as maximum intensity projections (MIP).

3.2 Effects of Sunitinib on [^{18}F]FAZA uptake in vivo

3.2.1 Effect of Sunitinib after 5 Days

Following characterization of the Caki-1 RCC model, [^{18}F]FAZA PET was used to detect potential functional changes during a short term (5 days) therapy with the TKI sunitinib. After 23 days of tumor growth BALB/c nu/nu mice carrying 2 subcutaneous Caki-1 tumors on each upper flank received 5 days of 40 mg/kg/d of sunitinib i.p. (1% DMSO in saline). Under sunitinib therapy, a reduced tumor growth was observed when comparing the growth rate to the vehicle-treated mice in the control group. On day 28 and after 5 days of sunitinib-treatment the treated tumors reached a tumor volume of 318 ± 62 mm^3 (n=8) versus 447 ± 90 mm^3 (n=8; n.s.), respectively (Figure 16).

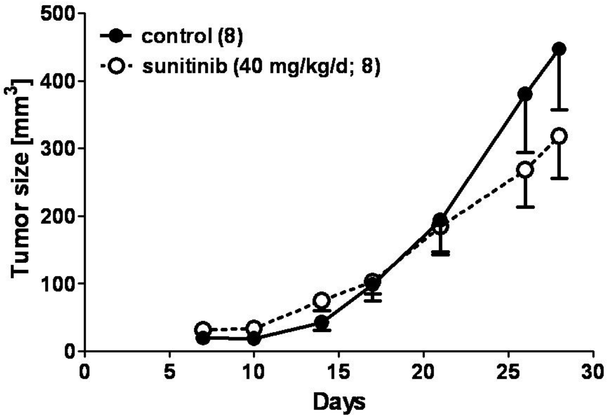

Figure 16: Effect of a 5 day sunitinib therapy on the tumor growth of subcutaneous Caki-1 tumors. Sunitinib therapy was started on day 23 and continued until day 28 of tumor growth.

On day 5 of treatment the mice were analyzed using dynamic small animal PET experiments acquiring data for up to 3 h p.i.. Figure 17 shows the [^{18}F]FAZA PET images as maximum intensity projections after 3 h p.i. for a control animal (left) and a sunitinib-treated animal (right). The insets show coronal slices of the tumor regions.

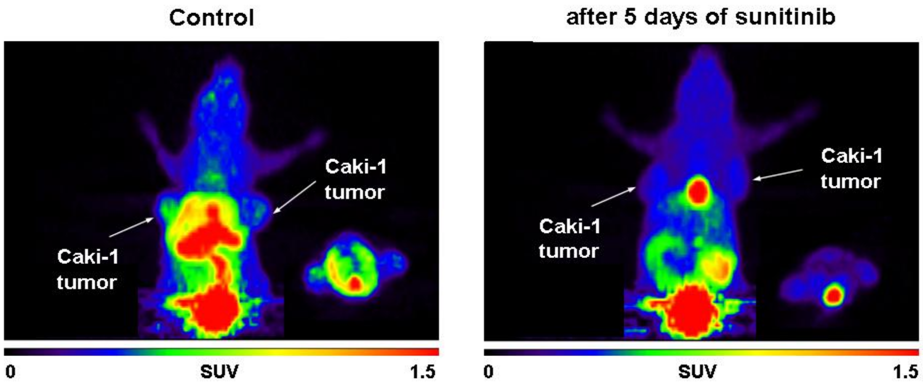

Figure 17: Uptake of [^{18}F]FAZA into control and sunitinib-treated Caki-1 tumor bearing mice at 3 h p.i.. Coronal sections are illustrated as insets in the bottom right-hand corner.

In the sunitinib-treated animals, a lower radiotracer uptake is visible in both Caki-1 tumors. Analysis of the tumor regions and generation of subsequent TACs revealed a different kinetic radiotracer profile for the tumor uptake in the treated versus the non-treated animals (Figure 18).

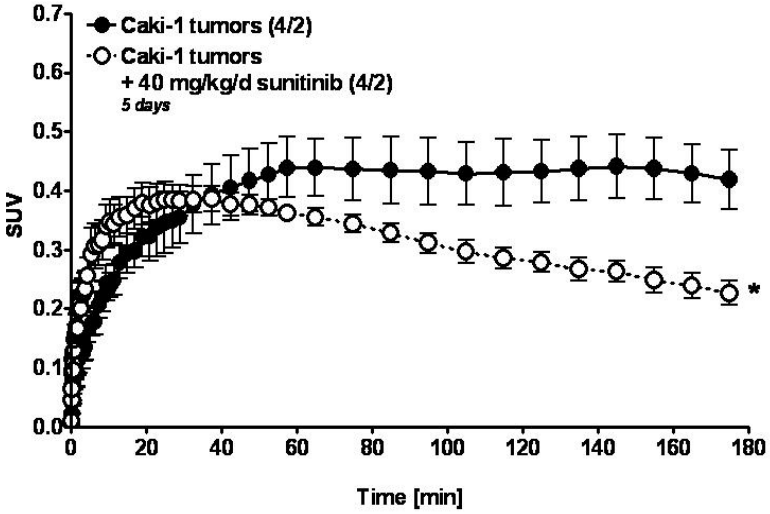

Figure 18: TACs for the tumor uptake for [^{18}F]FAZA into control and sunitinib-treated Caki-1 tumor bearing mice.

In control tumors, [^{18}F]FAZA uptake reached a maximum after 60 min p.i. with a SUV$_{mean}$ of 0.44 ± 0.05 (n=4/2) and remained relatively constant up to 3 h p.i. (0.42 ± 0.05 (n=4/2). In the sunitinib-treated animals radiotracer uptake into the Caki-1 tumors was reaching its maximum uptake at 30 min p.i. (SUV$_{mean}$ of 0.38 ± 0.02 (n=4/2) and decreased over the next 2.5 h to a final SUV$_{mean}$ of 0.23 ± 0.02 (n=4/2; $p < 0.05$) at 3 h p.i., respectively. This observation was indicative of a faster clearance of [^{18}F]FAZA from the tumor cells and therefore less trapping of the radiotracer and subsequently a lower level of hypoxia in the Caki-1 tumors after the animals were treated with sunitinib for 5 days.

Following the PET acquisition, mice were euthanized and tumor and muscle tissue were harvested and analyzed for their radioactivity content using a gamma-counter. Blood samples, liver tissue and kidneys were also collected, along with both Caki-1 tumors and the muscle tissue.

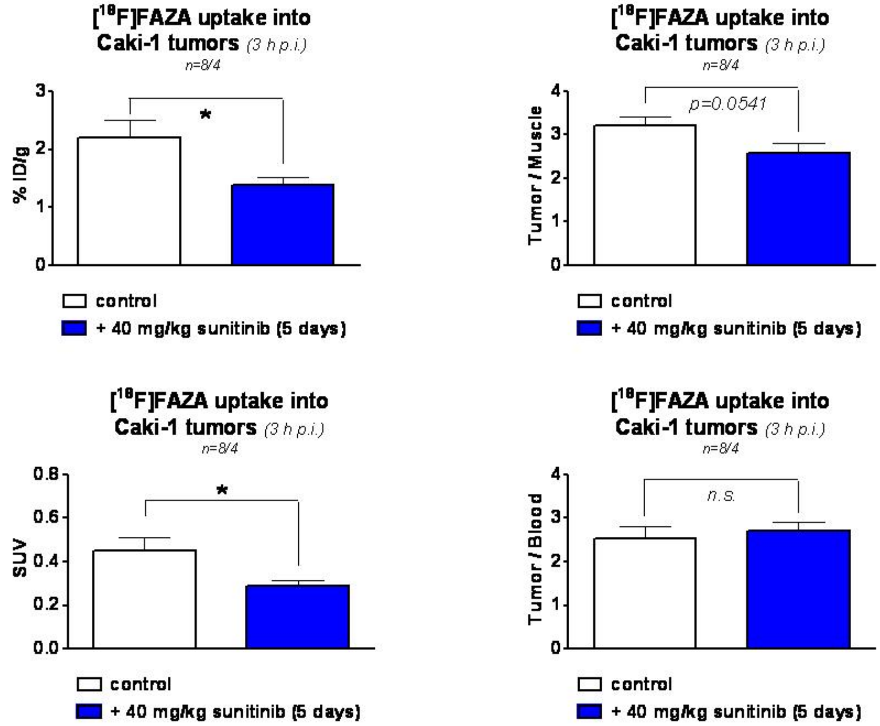

Figure 19: Results from the biodistribution experiments of the tumor tissue. Top left: tumor uptake as %ID/g; Bottom left: tumor uptake as SUV; Top right: tumor/muscle ratios; Bottom right: tumor/blood ratios from 8 tumors out of 4 animals per group.

Figure 19 summarizes the radioactivity amount in the tumor tissue as well as the tumor/muscle and tumor/blood ratios. Tumor uptake of [^{18}F]FAZA was significantly decreased in the sunitinib-treated animals: controls 2.20 ± 0.30 % ID/g versus sunitinib-treated 1.38 ± 0.13 % ID/g (n=8/4; $p<0.05$). The biodistribution data confirmed the results generated from the PET experiments. The tumor/non-tumor ratios were not statistically different in the treated animals, potentially due to the fact that the radiotracer clearance pattern was changed in the treated mice (Figure 20).

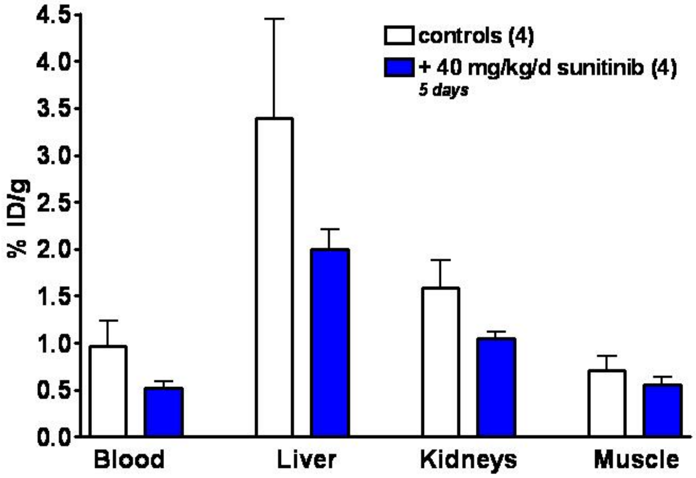

Figure 20: Results from the biodistribution in blood, liver, kidneys and muscle tissue. Data are shown as %ID/g from 4 animals per group.

Following PET experiments and biodistribution studies, tumor tissue was collected in formaldehyde, embedded in paraffin and tissue slices were prepared for immunohistochemistry. Pimonidazole staining was performed by injecting pimonidazole HCl into the tail vein 1 h before sacrificing the animal. Figure 21 shows two representative slices from Caki-1 tumor tissue, one from a control animal and the other one from a sunitinib-treated animal.

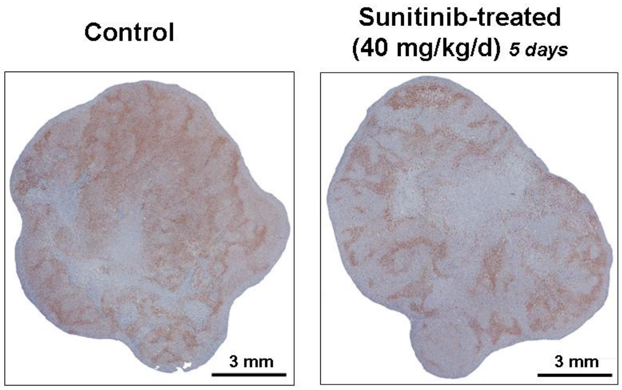

Figure 21: *Ex vivo* immunohistochemistry of sectioned tumor tissue comparing the staining of pimonidazole adducts in a vehicle-treated control (left) and a sunitinib-treated (40 mg/kg/d for 5 days) BALB/c nu/nu mouse (right).

Figure 22 shows the quantified immunohistochemistry data for the binding of pimonidazole as percent antibody binding and as means ± SEM from n analyzed tissue slices.

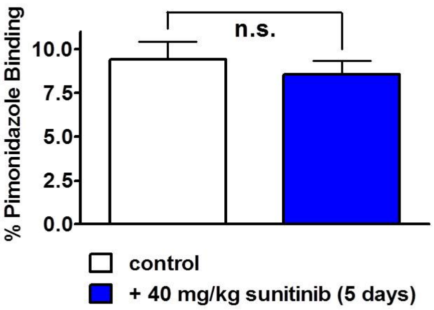

Figure 22: Quantified % binding of pimonidazole in Caki-1 tumors from vehicle-treated control animals and sunitinib-treated (40 mg/kg/d for 5 days) BALB/c nu/nu mice.

Like FAZA and MISO, pimonidazole is also a 2-nitroimidazole compound that binds to hypoxic cells based on passive diffusion into the cells and intracellular trapping under hypoxic conditions. In the samples examined here, no significant difference between tumor tissue from control (9.41 ± 1.04 % pimonidazole binding) versus sunitinib-treated

(8.55 ± 0.81 % pimonidazole binding; n=8/4; n.s.) animals was detected, although [^{18}F]FAZA was found to be significantly reduced. One reason may be that pimonidazole HCl was injected only one hour prior sacrificing the mice, while effects for [^{18}F]FAZA were determined after 3 h p.i., allowing for potential greater clearance of unbound drug

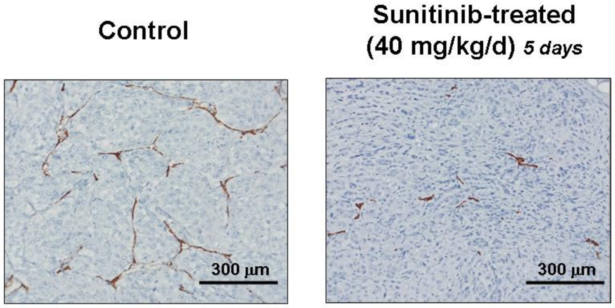

Figure 23: *Ex vivo* immunohistochemistry of sectioned tumor tissue comparing the staining the endothelial cell marker CD-31 in a vehicle-treated control (left) and a sunitinib-treated (40 mg/kg/d for 5 days) BALB/c nu/nu mouse (right).

CD-31 mAb is used as a marker for microvessel density. CD-31 is known as Platelet endothelial cell adhesion molecule and is expressed on the surface of platelets, monocytes, neutrophils, and some types of T-cells, and makes up a large portion of endothelial cell intercellular junctions. In the Caki-1 tissue from sunitinib-treated mice, CD-31 staining was clearly reduced. This observation was further confirmed when analyzing the quantified CD-31 staining data (Figure 24).

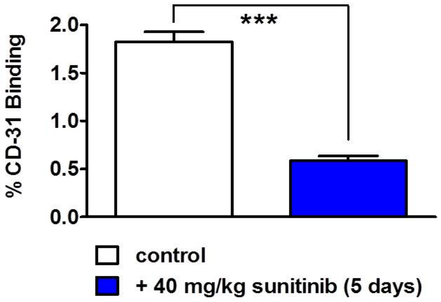

Figure 24: Quantified % binding of CD-31 in Caki-1 tumors from vehicle-treated control animals and sunitinib-treated (40 mg/kg/d for 5 days) BALB/c nu/nu mice.

In tumor tissue from control mice, 1.83 ± 0.10 % CD-31 binding was determined, whereas in the samples from sunitinib-treated animals the value was reduced to 0.58 ± 0.05 % CD-31 binding (n=8 tumors from 4 mice; $p < 0.001$). This finding indicates a reduced vessel density in the Caki-1 tumors during sunitinib-treatment.

3.2.2 Effects of Sunitinib during 15 Days

Following the investigation of the short term effects of sunitinib on tumor oxygenation, a second experimental set up was performed in order to analyze the longitudinal effects of anti-angiogenic therapy on Caki-1 tumor oxygenation. Thirty BALB-c/nu nu mice were inoculated with subcutaneous tumors on the upper left and right flank, and the tumors were allowed to grow for 13 days. Mice were then designated to either sunitinib-receiving or vehicle-treated (control) groups.

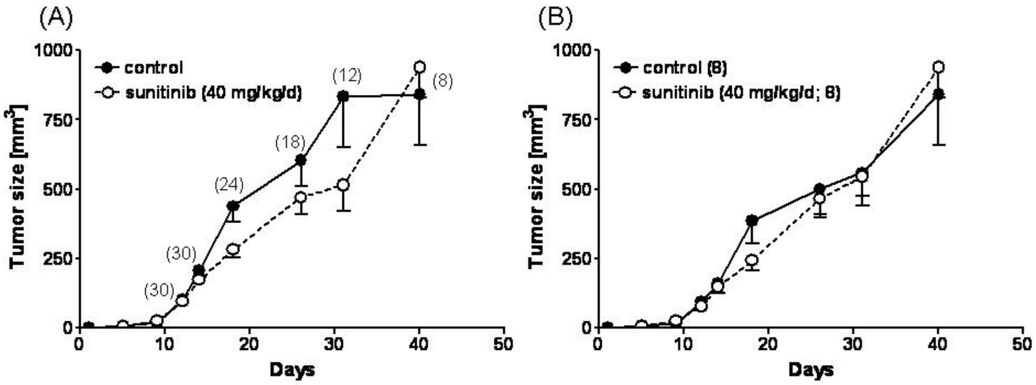

Figure 25: Effect of a 15 day sunitinib therapy followed by a 12 day period of therapy withdrawal on the tumor growth of subcutaneous Caki-1 tumors. Sunitinib therapy was started on day 13 and ended on day 28. A) all animals in the study; B) the 8 animals, which were receiving the entire treatment protocol and used at the end of the study.

Mice received 15 days of 40 mg/kg/d of sunitinib therapy i.p. and treatment was withdrawn for 12 days afterwards. Figure 25 presents the tumor growth rates for all animals in the study (left) and only the 8 animals, which were receiving the entire treatment protocol and kept until the end of the experimental setup at day 40 (right). Under the sunitinib therapy tumor growth was reduced compared to the control tumors, however, when therapy was withdrawn, the sunitinib-treated Caki-1 tumors grew faster again and reached similar sizes as the control tumors after 40 days.

Static PET experiments were performed at day 4 and day 9 of the sunitinib-therapy regimen. Representative images for both treatment options are shown in Figure 26. The Caki-1 tumors in the control animals clearly possess a higher radioactivity uptake level than the tumors in the sunitinib-treated animals, confirming again that in the presence of this TK inhibitor the amount of tumor hypoxia is decreased in the tumor's microenvironment.

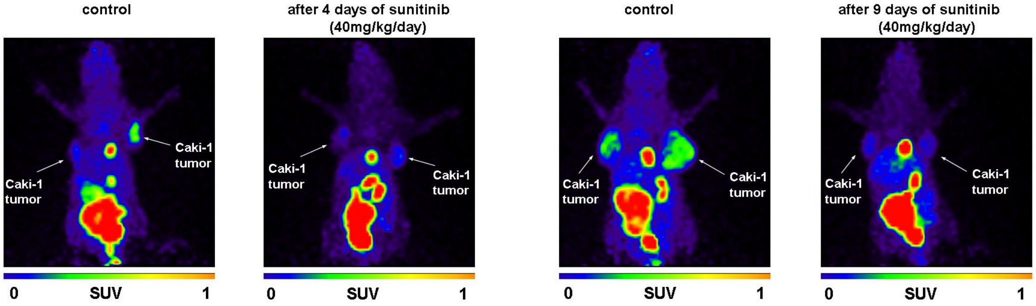

Figure 26: Representative PET images for [^{18}F]FAZA in Caki-1 tumor-bearing BALB/c nu/nu mice. Left: A control and sunitinib-treated mouse (4 days treatment) after 3 h p.i.; Right: Again a control and a sunitinib-treated mouse (9 days of treatment) after 3 h p.i..

Figure 27 shows the semi-quantified PET data for the uptake of [^{18}F]FAZA comparing both the sunitinib-treated and vehicle-treated BALB/c nu/nu mice bearing Caki-1 tumors. Uptake values were determined by defining a region of interest (ROI). It was found that sunitinib's effect on the tumor oxygenation was not yet significant after only 4 days of therapy, although the trend was evident, confirming the findings of the first study over 5 days (see 3.2.2). After 9 days of therapy, the $SUV_{mean,3h}$ of control tumors was found to be 0.24 ± 0.02, while the $SUV_{mean,3h}$ of sunitinib-treated tumors was 0.19 ± 0.01 (n=8; $p < 0.05$).

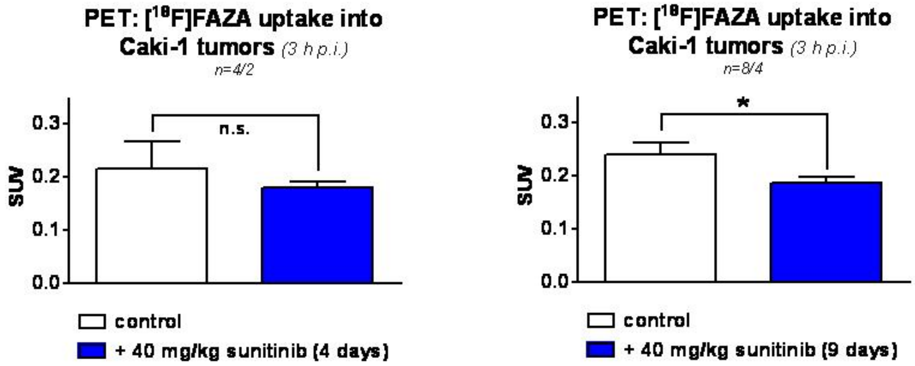

Figure 27: Semi-quantified PET data for the for uptake of [^{18}F]FAZA into Caki-1 tumors of control versus sunitinib-treated BALB/c nu/nu mice. Left: after 4 days treatment Right: after 9 days of treatment. Data are shown as mean ± SEM from n tumors out of x (n/x) animals at 3 h p.i. of the radiotracer.

Figure 28 shows the results from the biodistribution experiments at day 4 (left column), day 9 (middle column), and day 15 (right column). Tumors were harvested directly after the PET scans at 3 h p.i., at which time point their masses were determined and radioactivity counted using a gamma counter. The data is presented in both %ID/g (top row) and SUV (bottom row). Although statistical significance was not reached, the trend illustrating reduced uptake of [^{18}F]FAZA in sunitinib-treated tumors persisted at all three time points. After 4 days of therapy, uptake of [^{18}F]FAZA was found to be 1.50 ± 0.75 %ID/g in control tumors, and 0.75 ± 0.08 in sunitinib-treated tumors (n=4; n.s.). After 9 days of therapy, the trend was less obvious as uptake of [^{18}F]FAZA was more similar between control and sunitinib-treated mice. After 15 days of therapy, uptake of the radiotracer was found to be 1.08 ± 0.13 %ID/g in control tumors versus 0.93 ± 0.03 %ID/g in sunitinib-treated tumors (n=6; n.s.), respectively.

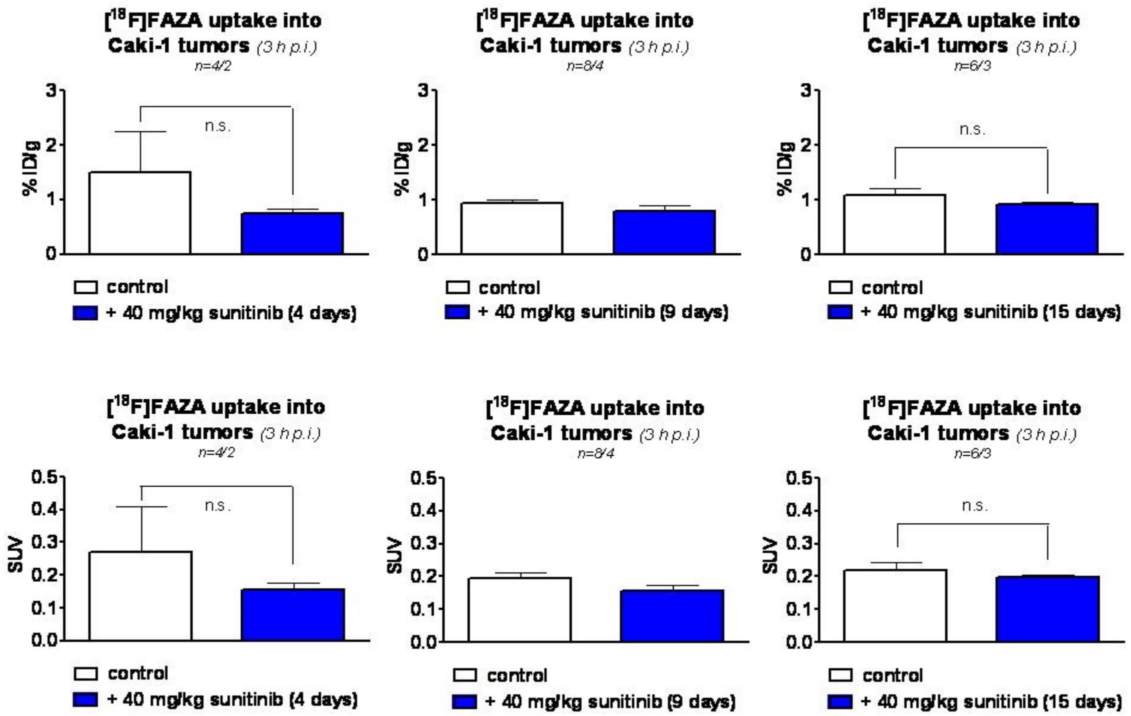

Figure 28: Results from the biodistribution experiments of the tumor tissue during the long-term therapy. Top row: tumor uptake as %ID/g; bottom row: tumor uptake as SUV; Left: effects of 4 days of sunitinib therapy; Middle: effects of 9 days of sunitinib treatment; Right: effects of 15 days of sunitinib therapy. Data are shown as mean ± SEM from n tumors out of x animals at 3 h p.i. of the radiotracer.

Figure 29 illustrates the results from *ex vivo* analysis of the immunohistochemical staining of tissue slides. Pimonidazole adducts were detected using IHC after 4 days and 15 days of sunitinib therapy and quantified using morphometric analysis. In contrast to the 5-day sunitinib therapy in the first experimental set-up (see 3.2.2.), pimonidazole HCl was injected i.p. 3 h prior to sacrifice of the animals. This change in methods was justified by the analysis of the TACs generated for [^{18}F]FAZA (Figure 18), because after 1 h p.i. no difference between the tumor uptake from controls and sunitinib-treated mice was detectable. The left graph in Figure 29 shows a trend for reduction in pimonidazole binding following 4 days of sunitinib therapy, where the sunitinib-treated tumor group showed 0.38 ± 0.10 % pimonidazole binding, and the vehicle-treated control tumor group showed 6.47 ± 2.96 % binding (n=8; p=0.087). Following 15 days of sunitinib therapy, pimonidazole binding between both groups was not significantly different, however, it showed a tendency for a lower pimonidazole uptake. It was then investigated whether withdrawing TKI therapy for 12 days would exhibit any changes in tumor oxygenation status.

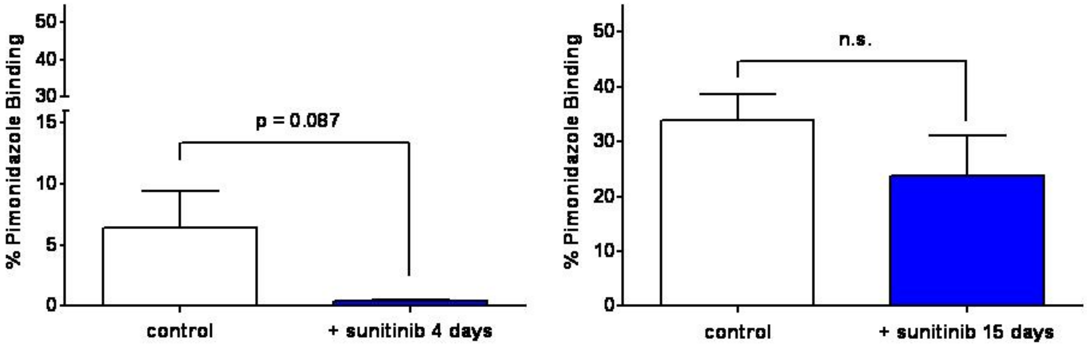

Figure 29: Quantified % binding of pimonidazole in Caki-1 tumors from vehicle-treated control animals and sunitinib-treated (40 mg/kg/d) BALB/c nu/nu mice. Left: after 4 days of therapy; Right: after 15 days of therapy.

3.2.3 Observations after Interruption of the Sunitinib Therapy

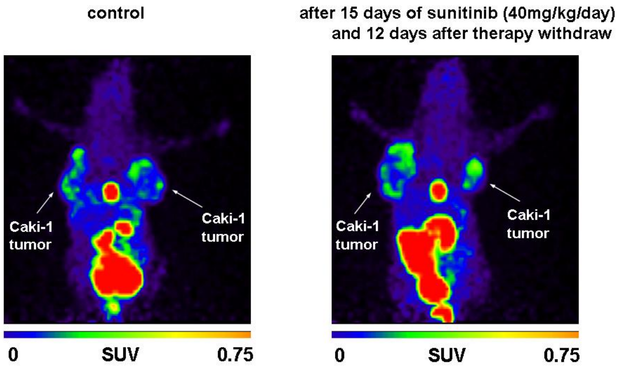

Figure 30: Representative PET images for [^{18}F]FAZA in Caki-1 tumor-bearing BALB/c nu/nu mice. Left: Control mouse; Right: A sunitinib-treated mouse (15 days treatment and 12 days after therapy withdrawal) after 3 h p.i.

Twelve days after sunitinib therapy was withdrawn, [^{18}F]FAZA PET experiments were performed at 3 h p.i. Qualitatively, no reduction of radiotracer uptake in the treated animals was observed anymore. Figure 30 shows maximum intensity projections at 3 h p.i., with the left image showing the vehicle-treated control mouse, and the right image showing a mouse that has received 15 days of sunitinib therapy following additional 12 days without sunitinib treatment before PET was done.

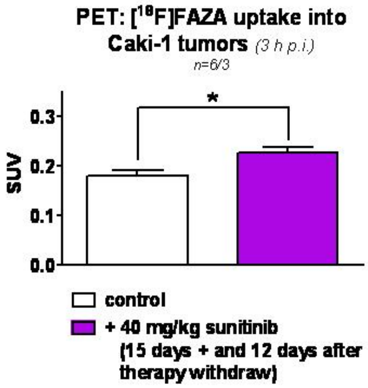

Figure 31: Semi-quantified PET data for the for uptake of [^{18}F]FAZA into Caki-1 tumors of control versus sunitinib-treated BALB/c nu/nu mice receiving 15 days of therapy plus 12 days after the therapy was withdrawn. Data are shown as mean ± SEM from N tumors out of x animals at 3 h p.i. of the radiotracer.

Analysis of the semi-quantified PET data revealed a $SUV_{mean,3h}$ of 0.18 ± 0.01 in the control tumors versus 0.23 ± 0.01 in the sunitinib-treated and therapy withdrawn tumors (n=6; $p<0.05$). Compared to the control group radiotracer uptake was significantly increased in the sunitinib-withdrawn tumors, indicating a flare effect in the Caki-1 tumor hypoxia status after withdrawal of sunitinib.

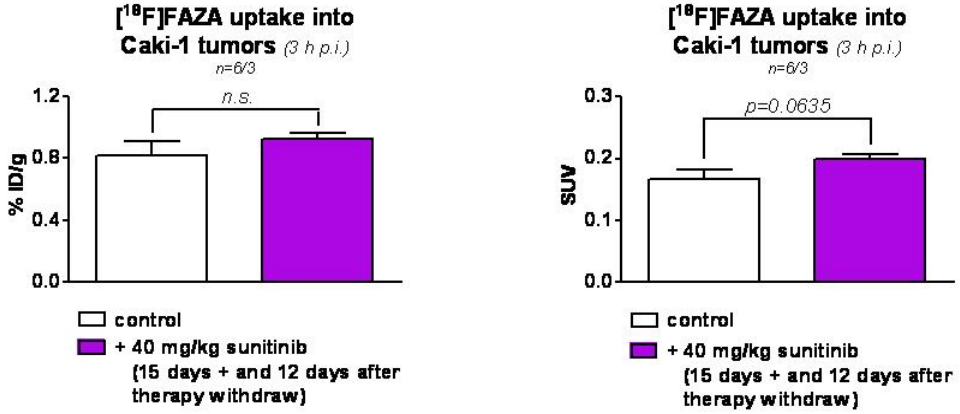

Figure 32: Results from the biodistribution experiments of the tumor tissue after 15 days of sunitinib therapy and 12 days following therapy withdraw. Left: tumor uptake as %ID/g; Right: tumor uptake as SUV. Data are shown as mean ± SEM from N tumors out of x animals at 3 h p.i. of the radiotracer.

Immediately following the PET acquisition, animals were sacrificed and tumor tissue was harvested, and radioactivity was determined in a gamma counter. Figure 32 shows a comparison of [^{18}F]FAZA uptake between sunitinib-therapy followed by therapy withdrawn animals and controls in %ID/g and SUV. Uptake of [^{18}F]FAZA was found to be 0.82 ± 0.09 %ID/g in controls versus 0.92 ± 0.04 in sunitinib-withdrawn tumors (n=6; n.s). The subsequent SUV values resulted in 0.17 ± 0.02 (controls) and 0.20 ± 0.01 (sunitinib animals; n=6; p=0.0635). Although the biodistribution results did not quite reach statistical significance, the trend was similar to what was observed in the statistical analysis of the semi-quantitative PET data.

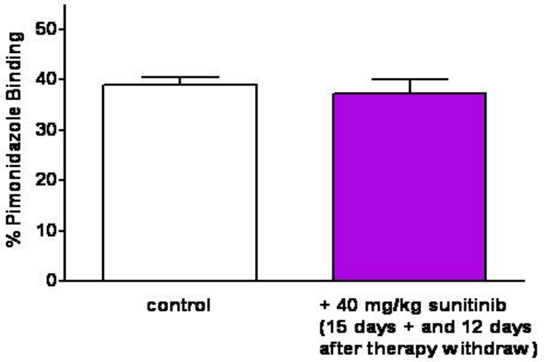

Figure 33: Quantified % binding of pimonidazole in Caki-1 tumors from vehicle-treated control animals and sunitinib-treated (40 mg/kg/d) BALB/c nu/nu mice after 15 days of sunitinib therapy and 12 days following therapy withdrawal.

Analysis of the immunohistochemical staining for pimonidazole adducts on paraffin-embedded tumor tissue samples resulted in similar % pimonidazole binding meaning no difference between control and sunitinib-treated following therapy withdrawal was detected. One observation was the marked difference in % pimonidazole binding in the samples that received sunitinib for 4 days, and 15 days compared to the % binding in the sunitinib-withdrawn tumors (received 15 days of 40 mg/kg/d and 12 days without treatment). Both the control and sunitinib-treated tumors near the end of the entire experimental setup for the long TKI treatment were much larger than at earlier time points (see Figure 25) and this may help explain this difference in % pimonidazole binding.

3.3 *In Vitro* Uptake Experiments

3.3.1 Hypoxia versus Normoxia

Radiotracer uptake of [^{18}F]FAZA and [^{18}F]FDG in the Caki-1 renal cell carcinoma cell line and the human breast cancer cell line MCF-7, was determined using a degassing system including vacuum, air-tight chambers, and nitrogen gas supply (5% CO_2). Figure 34 shows the uptake of [^{18}F]FAZA and [^{18}F]FDG in both cell lines under both oxygen conditions. Determining the cellular uptake of [^{18}F]FAZA after 4 hours of incubation in both cell lines, revealed an uptake of 0.24 ± 0.02 (n=6) in Caki-1 cells and 0.37 ± 0.06 % radioactivity/mg protein into MCF-7 cells (n=10) under normoxic conditions. Caki-1 and MCF-7 radiotracer uptake under hypoxic conditions was found to be 2.42 ± 0.09 (n=6; $p<0.001$ vs. normoxic uptake) in Caki-1, and 2.63 ± 0.44 (n=10; $p<0.001$ vs. normoxic uptake) in MCF-7 cells. Cellular trapping of [^{18}F]FAZA in Caki-1 cells was increased approximately 10-fold under hypoxic conditions, while MCF-7 exhibited an approximately 8-fold increase in radiotracer uptake (Figure 34) indicating that [^{18}F]FAZA is trapped in both cell types under hypoxic conditions.

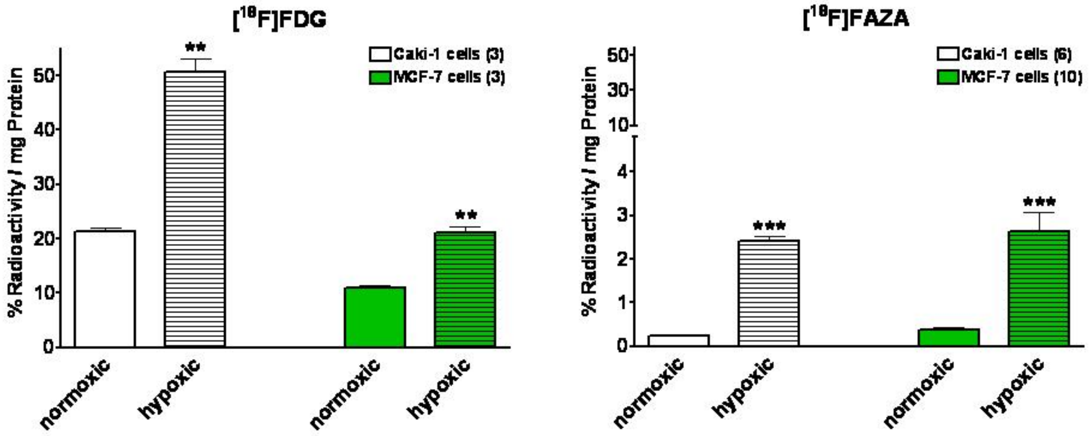

Figure 34: Cell uptake of [^{18}F]FDG (left) and [^{18}F]FAZA (right) into Caki-1 cells (human RCC cell line) and MCF-7 cells (human mammary carcinoma cell line) under normoxic and hypoxic conditions. Data are shown as mean ± SEM from n experiments and after 1 h ([^{18}F]FDG) or 4 h ([^{18}F]FAZA) incubation time.

Furthermore, [^{18}F]FDG uptake was also analyzed in both cell lines under normoxic and hypoxic conditions (Figure 34). In the Caki-1 cells, uptake of [^{18}F]FDG was found to be 21.4 ± 0.7 % radioactivity/mg protein under normoxic conditions, and it increased approximately 2-fold under hypoxic conditions to 50.6 ± 2.5 % radioactivity/mg protein ($p<0.001$). Similarly, MCF-7 uptake of [^{18}F]FDG was found to increase nearly 2-fold from 11.1 ± 0.3 to 21.0 ± 1.2 % radioactivity/mg protein ($p<0.001$). This finding indicates an increase in glucose metabolism in these cell lines under hypoxic conditions.

3.3.2 Effect of Sunitinib on [^{18}F]FAZA Cell Uptake

Once the hypoxia-specific activation and trapping of [^{18}F]FAZA into Caki-1 and MCF-7 cells was established *in vitro,* a potential direct compound effect of sunitinib on this activation process was investigated. Using the same degassing system, the uptake and trapping of [^{18}F]FAZA was determined in Caki-1 and MCF-7 cell lines in the presence of

3 μM sunitinib under both normoxic and hypoxic conditions (Figure 35). This concentration for sunitinib was selected to ensure the concentration was well above the minimum concentration to completely inhibit sunitinib's targets. Under normoxic conditions, [^{18}F]FAZA uptake into Caki-1 cells was found to be 0.25 ± 0.04 in the absence and 0.22 ± 0.04 (n=3) in the presence of 3 μM sunitinib. Under hypoxic conditions, [^{18}F]FAZA uptake was found to be 2.46 ± 0.42 in the absence and 2.42 ± 0.36 (n=3) in the presence of sunitinib.

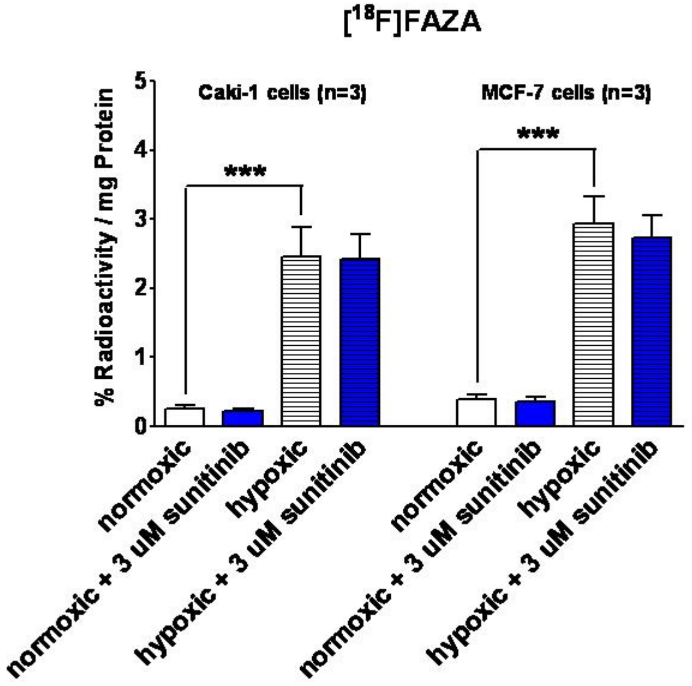

Figure 35: Effects of 3 μM sunitinib on the cell uptake of [^{18}F]FAZA into Caki-1 cells (left) and MCF-7 cells (right) under normoxic and hypoxic conditions. Data are shown as mean ± SEM from n experiments after 4 h incubation time.

Furthermore, in the MCF-7 cell line under normoxic conditions, radiotracer uptake was found to be 0.39 ± 0.07 and 0.36 ± 0.05 % radioactivity/mg protein (n=3) in the absence and presence of 3 μM sunitinib. Under hypoxic conditions, [^{18}F]FAZA uptake increased to 2.94 ± 0.38 and 2.73 ± 0.33 % activity/mg protein (n=3; n.s.) in the absence and presence of 3 μM sunitinib, respectively. From these experiments it can be concluded that sunitinib had no effect on the mechanism of trapping of [^{18}F]FAZA in both cell lines (Caki-1 and MCF-7) indicating that the drug effects on the tumors as observed *in vivo* are not related to any effect of the TKI sunitinib on the tumor cells.

Chapter 4: Discussion and Conclusion

Following the completion of these radiotracer experiments, there are 4 main findings that can be summarized upfront: 1) The Caki-1 RCC subcutaneous tumor model exhibits uptake of [^{18}F]FAZA and is suitable to examine the effects of sunitinib on the tumor's oxygenation status; 2) Short-term (5 days) sunitinib therapy resulted in a decrease in [^{18}F]FAZA uptake, indicating a reduction of tumor hypoxia; 3) A TKI withdrawal flare phenomenon was observed 12 days following cessation of sunitinib therapy for 12 days resulting in a higher [^{18}F]FAZA uptake, again indicating an increase in tumor hypoxia; 4) A high concentration of sunitinib (3 μM) did not have a direct effect on the cellular uptake and retention of [^{18}F]FAZA in Caki-1 and MCF-7 cells under normoxic or hypoxic conditions in cell culture.

Renal cell carcinoma (RCC) continues to be one of the leading causes of mortality among urological malignancies, with up to 38% of patients presenting with metastatic disease. With the development of tyrosine kinase inhibitors, physicians can now manage metastatic renal cell carcinoma more like a chronic disease, taking into consideration more than just the oncological outcomes but also the renal function and other patient comorbidities.[2] Unfortunately, treatment resistance against TKIs results from chronic therapy, and eventually there is a loss of tumor growth inhibition and a flare-up phenomenon, where tumors show accelerated rates of proliferation, is sometimes observed.[150,151] Tumor hypoxia has been investigated in several pre-clinical models and clinical studies, and it has been found to be associated with a lack of response to conventional chemotherapy such as cisplatin, radiotherapy, and immunotherapy with interferon-α or interleukin-2, along with elevated metastatic potential, which has led scientists to further investigate the effects of anti-angiogenic agents such as TKIs on tumor oxygenation and vascularity. Conflicting evidence has been discovered, however, from several studies finding that TKI's induce intratumoral hypoxia, while others have found that TKI's lead to an improvement in tumor oxygenation.[5,146,147,152] Based on these conflicting results, it seems to be clear that the therapeutic effects of TKI's may be based on multiple factors, and the overall effect could vary on the specific TKI being used, the administered dose, the particular tumor model and RCC cell type, and finally the duration of the TKI therapy. Improving the ability to non-invasively image tumor hypoxia would be extremely valuable for a number of reasons: A) it could help with the detection of distant metastasis; B) allow monitoring of individualized patient response to specific therapies; and C) it could be used to guide potential combination therapies including bioreductive cytotoxins such as tirapazamine, or together with conventional chemotherapy and radiotherapy. This particular project focused on using the PET radiotracer [^{18}F]FAZA to non-invasively detect any changes in tumor hypoxia during and after therapy with a TKI, sunitinib, in a human-xenograft RCC mouse model.

Prior to determining whether [^{18}F]FAZA could be used to detect any changes in tumor oxygenation following TKI therapy, characterization of the Caki-1 RCC mouse model with both radiotracers [^{18}F]FDG (metabolism) and [^{18}F]FAZA (hypoxia) was performed. In the present experiments, it was found that the uptake of [^{18}F]FDG reached an $SUV_{mean,1h}$ of 0.60. Ambrosini *et al.* found a similar $SUV_{mean,1h}$ of 0.6 for [^{18}F]FDG in

L248 tumors (human Hodgkin lymphoma), while in Karpass 299 tumors (human T cell lymphoma) the $\mathrm{SUV}_{\mathrm{mean,1h}}$ reached an SUV of 1.[153] An $\mathrm{SUV}_{\mathrm{mean,1h}}$ of 1.1 was also measured in A2780 tumors (human ovarian cancer model).[151] In the murine mammary tumor model EMT-6, an $\mathrm{SUV}_{\mathrm{mean,1h}}$ of 1.6 was detected, while in the human xenograft mammary MCF-7 model a value of only 0.8 is found.[154] So far, no pre-clinical study could be found reporting a SUV for the uptake of [^{18}F]FDG into a RCC mouse tumor. Compared to the values from the literature, the Caki-1 xenograft RCC tumor model exhibits a lower metabolic rate, comparable to the one in MCF-7 and L248 tumors, while others show a much higher metabolism rate. Utilizing [^{18}F]FAZA PET in untreated Caki-1 tumors also revealed a relatively low tumor uptake compared to what others have previously reported. Specifically, the $\mathrm{SUV}_{\mathrm{mean,3h}}$ of 0.32 in Caki-1 tumors was lower compared to the tumor uptake of other cell lines including A431, CT26, polyomavirus middle-T (PyV-mT) mammary carcinoma, EMT6, and AR42J.[155-157] Comparable to the Caki-1 model, Murakami *et al.* found a very low uptake of [^{18}F]FMISO in A498, another human RCC xenografted tumor model.[158] Based on the literature, RCC tumors are characterized by having elevated interstitial fluid pressure that could potentially explain the lower uptake in RCC tumors relative to other tumor types which potentially have a lower interstitial fluid pressure.[149] In addition to the subcutaneous Caki-1 tumor mouse model, the orthotopic Caki-1 kidney tumor model was also investigated, but based on the visual uptake and clearance patterns of [^{18}F]FAZA in the PET images alone, the tumors could not be identified without a structural input from CT functionality.

Techniques for determining tumor oxygenation including invasive oxygen sensing probes, immunohistochemical detection of pimonidazole adducts, various PET radiotracers including [^{18}F]FAZA, [^{18}F]FMISO as well as SPECT tracers such as [^{123}I]IAZA or ^{99m}Tc-HL91, and MRI have been used.[157,159-162] PET is an ideal tool to use for this as it has high spatial resolution, high sensitivity, and is able to measure functional processes in the body as a non-invasive method. Two similar radiotracers frequently studied include the 2-nitroimidazoles [^{18}F]FAZA and [^{18}F]FMISO. Both PET tracers exhibit the same mechanism of activation and specificity for hypoxia, however, [^{18}F]FAZA has been shown to possess a faster clearance *in vivo* based on its lower lipophilicity. This leads to improved clearance from non-hypoxic tissue and excretion, making it a more favorable tracer by improving the tumor to background ratio.[160] Interestingly enough, the tumor type also plays a role in the selection of a suitable tracer. [^{18}F]FMISO uptake (SUV=4.6±1.8) has been shown to be superior to [^{18}F]FAZA (SUV=3.0±0.5) in a rat sarcoma model, which emphasizes the different characteristics of cancer cell lines.[160] Pimonidazole HCl is the most studied 2-nitroimidazole compound, however it has several limitations. It can only be detected *ex vivo*, limiting its use to invasive tissue biopsies, which is rarely a true representation of the overall sample. There is also some discrepancy in the literature about its use in pre-clinical models related to how long before the tumor tissue collection the agent has to be injected. Based on the chemical structure and properties of pimonidazole and the TAC for [^{18}F]FAZA determined in Caki-1 tumors during this study (Figure 9), pimonidazole HCl should be injected at least 3 hours prior to tissue collection for a more optimal result. Depending on the expected effect, timing may vary as other studies have used just 1 h injection time prior tissue collection.[5] However, pimonidazole has a lipophilicity similar to that of [^{18}F]FMISO, requiring a greater amount of time to clear from non-hypoxic tissue. Furthermore, pimonidazole HCl binding has been shown to be pH dependent, suggesting that it may not be a true representation of the tumor's oxygenation status only.[163] Many groups have investigated different strategies to modify tumor oxygenation, and the present project has focused on a therapeutic intervention with a TKI inhibitor to induce changes in the tumor microenvironment.

In the present work, Caki-1 tumors were grown subcutaneously in BALB/c nu/nu mice as a pre-clinical model. Using dynamic PET, it was demonstrated (Figure 9) that there is a faster clearance of [^{18}F]FAZA from sunitinib-treated tumors when compared to the control tumors. These results were then validated through *ex vivo* biodistribution studies (Figure 10) from the harvested tumor tissue. Furthermore, immunohistochemical staining for pimonidazole adducts was also performed and showed a similar trend. In addition to immunohistochemical detection of pimonidazole adducts, CD-31, an endothelial cell marker was also studied. Following short-term therapy, there was a drastic reduction in CD-31 binding, indicating a decrease in vascular density. It has previously been examined whether tumors receiving TKI therapy experience a change in tumor oxygenation and vascular density. Most clinical studies analyzing TKI therapy in RCC tumor patients have found that under therapy the tumor vasculature would normalize, leading to an improved tumor blood supply following reduction in tumor metabolism and proliferation rate as well as a decrease in tumor hypoxia status.[146,150,164-169] However, some other, mostly preclinical, studies have found evidence that TKIs would induce tumor hypoxia.[5,152,158] It is apparent there are two conflicting opinions on the overall effect of anti-angiogenic therapy. It was first thought that these agents lead to cancer cell death by preventing the development of new blood vessels (neo-angiogenesis) or destruction of already-established blood vessels, ultimately leading to starvation.[170] A more recent observation actually shows a repair in tumor vascular abnormalities including attenuation of hyperpermeability, increased vascular pericyte coverage, a more normal basement membrane, and a reduction of hypoxia and interstitial fluid pressure (IFP).[149] Many recently published articles show a number of different techniques for measuring intratumoral hypoxia and the contrasting effects of TKI therapy on the tumor's oxygenation status in different tumor models.

Gaustad *et al.* studied the effects of sunitinib on vascular morphology and function, as well as the hypoxic fraction in melanoma cell lines. They used immunohistochemical detection of intracellular pimonidazole adducts and intravital microscopy to observe changes in vascular morphology and function.[152] Although Gaustad and co-workers also found a significant decrease in vascular density following sunitinib therapy, they detected an induction of hypoxia in their particular cell lines using the same dose of sunitinib (40 mg/kg/day) for 1 to 4 days. In the present study, no repair of vascular function was seen and this suggests that neoadjuvant therapy with sunitinib could potentially decrease the efficacy of ionizing radiation or chemotherapy in these particular cell lines.[152]

Additionally, Welti *et al.* investigated the contrasting effects of sunitinib on vascular density and hypoxia in different cell lines. They compared two metastasizing cell lines, RENCA and 4T1, and found that treating 4T1 tumor-bearing mice, resulted in increased tumor hypoxia, while this effect was not observed in the RENCA cell line.[171] Furthermore, it was found that tumor growth was not inhibited by sunitinib in 4T1, while it was inhibited in the RENCA model. This finding clearly suggests that all cell lines respond differently to sunitinib therapy, and a broader array of cell lines and tumor models should be examined. This observation of tumor heterogeneity highlights the importance of a fast, non-invasive technique for monitoring unique patient-specific tumor response to particular therapies.[171] Alarmingly, it has also been found that anti-angiogenic agents increase the number of cancer stem cells through the induction of hypoxia in solid tumors. It is suggested that hypoxia and hypoxia-related gene activation could potentially be involved in all steps of metastasis including the initial epithelial-mesenchymal transition to colonization.[172] Following 60 mg/kg of sunitinib, it was found that this treatment induced tumor hypoxia in breast cancer cells and increased the number of cancer stem cells (determined by Aldefluor+).[173] Combining cancer stem cell targeting therapies with anti-angiogenic agents could be investigated in particular cell lines. Unfortunately, the present study was conducted over a span of just a few weeks and tumors were implanted subcutaneously, so lymph node metastasis could not be detected in this time period and in this particular animal model. Unpublished data from our laboratory using an orthotopic kidney tumor shows a decrease in the number of lymph node metastasis following sunitinib, sorafenib, and temsirolimus therapy on Caki-1 cell line. This contradicts many publications finding an increase in metastasis following anti-angiogenic therapy and may be explained by the different responses of each cell line to the therapy with TK inhibitors.

It is well known that all of the available TKIs exhibit a different spectrum of affinities to different receptors in the cell and that this plays a significant role in the overall compound effect. Sunitinib was originally designed to specifically inhibit VEGFR, PDGFR and C-kit, however, it has been found to inhibit other types of kinases as well including non-receptor tyrosine kinases, receptor tyrosine kinases, tyrosine kinase-like kinases, cyclin-dependant kinases, and mitogen-activated protein kinase, among many others.[174] For this reason, it is reasonable to assume that sunitinib as a type I TKI has a greater number of off-target effects compared to some of the more specific TKI's categorized as type II such as sorafenib and imatinib. This may help explain the contrasting effects observed in different cell lines following TKI therapy. Fabian *et al.* examined the specificity profiles of TKIs including sunitinib, sorafenib and some others.[174] Sunitinib was shown to inhibit 73 kinases in addition to its primary target, VEGFR-2.[174] In addition to the vastly different binding affinities of TKIs to their primary target and off-targets, varying cellular expression of the tyrosine kinases also plays a role in the overall effect of the therapy. Specifically, it has been shown that, between many RCC cell lines, the expression of VEGF can differ greatly.[175] Comparing the RCC cell line A498 utilized by Murakami *et al*., and Caki-1 cell line used in the present experimental setup, A498 had a 4-5 time greater VEGF production.[158]

The administered dose and therefore bioavailability also has been shown to play a factor in the modification of tumor hypoxia. Sun *et al.* compared the effect of a 20 mg/kg/d with a 40 mg/kg/d dose for 5 days and found that only the 40 mg/kg/d dose was able to induce hypoxia.[176]

The purpose of the present study was to determine the ability of [^{18}F]FAZA PET to detect early response to sunitinib therapy in a renal cell carcinoma model. [^{18}F]FAZA PET has previously been used to monitor the response of A431 squamous cell carcinoma xenografts to the epidermal growth factor receptor inhibitor, gefitinib.[141] Similarly to a sunitinib therapy in Caki-1 cells, it was found that following short-term gefitinib therapy (5 and 8 days), [^{18}F]FAZA uptake was reduced indicating improved tumor oxygenation.[141] Dorow *et al.* also monitored therapeutic response of A431 to CI-1033, a pan-erb-B inhibitor, using several PET tracers including [^{18}F]FDG, [^{18}F]FLT, and [^{18}F]FAZA.[177] It was found that there was a significant reduction of up to 60% for [^{18}F]FDG and [^{18}F]FAZA uptake after 3 and 7 days of therapy as analyzed from the tumor to background ratios. In addition, [^{18}F]FMISO was also utilized to monitor the therapy effect. Radiotracer tumor uptake and effects of CI-1033 were similar with both [^{18}F]FAZA and [^{18}F]FMISO. To date, these two studies seem to be the only ones that have utilized [^{18}F]FAZA to monitor TKI therapeutic response.[177] Revheim *et al.* have investigated the use of positron emission tomography with [^{18}F]FDG to monitor the effect of a targeted TKI therapy.[165] Sunitinib- and imatinib-treated mice bearing GIST xenografts showed significantly lower tumor-to-liver uptake of [^{18}F]FDG than the control mice, indicating a decrease in glucose utilization during sunitinib and imatinib therapy. Interestingly, sunitinib (type I TKI) had a greater effect with 54% change compared to 40% observed with imatinib (type II TKI). However, the authors did not analyze this observation nor determine the difference in more detail.

The withdrawal flare phenomenon is something that has not been thoroughly investigated following cessation of anti-angiogenic therapy. In the present experimental set-up, [^{18}F]FAZA PET was used to measure tumor hypoxia during, and following treatment cessation. Under treatment, it was found that tumor hypoxia was reduced, presumably by a reduction of tumor cell proliferation and decreased oxygen consumption, along with normalization of tumor vasculature. Twelve days following a 3-week sunitinib therapy regime, [^{18}F]FAZA uptake was measured and it was found that there was an increase in radiotracer uptake, indicating a re-induction of tumor hypoxia. Following the release of TK inhibition, it has been shown that tumor cell activity rebounds and experiences accelerated proliferation.[150] In human renal cell cancer, Lui *et al.* utilized [^{18}F]FLT PET/CT to determine the rate of proliferation and it was found that SUV of [^{18}F]FLT increased by 15% (p=0.047) after sunitinib withdrawal. This may indicate that the rate of oxygen consumption could also have increased, resulting in further imbalance of the supply and demand of oxygen to the cells. Currently, patients receive sunitinib at a dose of 50 mg/kg/d for 4 weeks and then 2 weeks off, however other regimes are being investigated including 2 weeks on and 1 week off. Following treatment cessation, patients sometimes experience recurrent pain in metastatic sites, as a result of flare re-growth. It has also been proposed that during this period of withdrawal, tumor cells are stuck in "S" phase and therefore are more vulnerable to combination cytotoxic chemotherapy.[150]

After determining a reduced uptake of [^{18}F]FAZA in the Caki-1 tumors, *in vitro* studies were conducted in order to determine if sunitinib could directly interfere with the uptake and trapping mechanism of [^{18}F]FAZA, in other words, possess a direct compound effect on the Caki-1 cells. Using the mammary MCF-7 cell line as an experimental control to establish the right experimental conditions for a cell experiment under hypoxic conditions, uptake of [^{18}F]FAZA was determined under normoxic and hypoxic conditions in the presence and absence of 3 μM sunitinib. From the literature, it was shown that MCF-7 responded significantly to hypoxic conditions, exhibiting an almost 4-fold increase in [^{18}F]FMISO uptake compared to normoxic conditions.[178] Based on this, the MCF-7 cells were also used for comparison with the Caki-1 cell and their uptake of [^{18}F]FAZA. Comparing the MCF-7 uptake reported by Oswald *et al.* a similar cell uptake of [^{18}F]FAZA was found under both, the normoxic and hypoxic conditions, following a 4 hour incubation with [^{18}F]FMISO. Sunitinib (3 μM) did not influence the uptake of [^{18}F]FAZA indicating that this TKI has no direct effect on both tumor cell lines at least up to the analyzed concentration, which is greater than the average or peak serum concentration in patients. The observed therapeutic effects *in vivo* would therefore solely result from the effect of sunitinib on the blood vessels which influence the blood flow and oxygen supply to the tumor cells or by proliferation effects. However, based on several aspects discussed here, the overall summary effect of sunitinib as a type I TK inhibitor targeting multiple enzymes and receptor systems may represent a summary effect and cannot be contributed to a simple targeting effect on VEGFR2 in vascular endothelial cells only.

Conclusion:

Based on the presented results, it can be concluded that PET as a non-invasive imaging technique utilizing [^{18}F]FAZA can be used to detect functional changes in the tumor's microenvironment (hypoxia) of a metastatic renal cell carcinoma mouse model, specifically in the Caki-1 model. It was found that during therapy with the tyrosine kinase inhibitor sunitinib, [^{18}F]FAZA uptake and trapping in Caki-1 tumors was reduced, indicating that tumor oxygenation was improved during TKI therapy in this specific experimental mouse model. Furthermore, upon withdrawal of sunitinib therapy, [^{18}F]FAZA uptake was found to increase again, demonstrating a rebound in tumor hypoxia. Since other radiotracers such as [^{18}F]FDG, [^{18}F]FLT and [^{18}F]FMISO have previously been used to monitor TKI therapy in RCC patients in the clinic, this work has shown that [^{18}F]FAZA can also be used to monitor early response, long-term therapy and therapy withdrawal of a TKI drug therapy such as sunitinib. To further understand modification of tumor oxygenation properties as a result of a sunitinib therapy, several other radiotracers could also be evaluated in order to better characterize the overall functional changes in a specific preclinical RCC tumor model (Caki-1). Based on the literature, the overall effect of different TKIs may vary to some extent as a result of their vastly different specificities and their mechanism of action (Type I and Type II TKIs). It would be of interest to analyze different TKIs and their summary therapeutic effects *in vivo* in one particular preclinical model in order to generate comparable data for potential clinical protocols. To further understand the overall effect of particular TKI's in this specific RCC tumor model (Caki-1), also other PET radiotracers such as [^{18}F]FLT to measure tumor cell proliferation, [^{18}F]FDG to measure rate of metabolism, and ^{68}Ga-labeled RGD peptides to determine changes in the rate of angiogenesis could be investigated. Utilizing these radiotracers would allow the analysis of the effect of different TKIs on the balance of oxygen supply (angiogenesis and vascularity) and demand (oxygen consumption as a result of metabolism and proliferation).

References

1. Gupta K, Miller JD, Li JZ, Russell MW, Charbonneau C. Epidemiologic and socioeconomic burden of metastatic renal cell carcinoma (mRCC): a literature review. Cancer Treat Rev 2008;34:193-205.
2. Chapman D, Moore R, Klarenbach S, Braam B. Residual renal function after partial or radical nephrectomy for renal cell carcinoma. Can Urol Assoc J 2010;4:337-43.
3. Klarenbach S, Moore RB, Chapman DW, Dong J, Braam B. Adverse renal outcomes in subjects undergoing nephrectomy for renal tumors: a population-based analysis. Eur Urol 2011;59:333-9.
4. Chow LQ, Eckhardt SG. Sunitinib: from rational design to clinical efficacy. J Clin Oncol 2007;25:884-96.
5. Chang YS, Adnane J, Trail PA, et al. Sorafenib (BAY 43-9006) inhibits tumor growth and vascularization and induces tumor apoptosis and hypoxia in RCC xenograft models. Cancer Chemother Pharmacol 2007;59:561-74.
6. Voce P, D'Agostino M, Moretti S, et al. Sunitinib inhibits tumor vascularity and growth but does not affect Akt and ERK phosphorylation in xenograft tumors. Oncol Rep 2011;26:1075-80.
7. Chow WH, Dong LM, Devesa SS. Epidemiology and risk factors for kidney cancer. Nat Rev Urol;7:245-57.
8. Rini BI, Campbell SC, Escudier B. Renal cell carcinoma. Lancet 2009;373:1119-32.
9. Kidney Cancer. 2012. (Accessed December 2012, at http://www.cancer.gov/cancertopics/types/kidney.)
10. Cohen HT, McGovern FJ. Renal-cell carcinoma. N Engl J Med 2005;353:2477-90.
11. Tsui KH, Shvarts O, Smith RB, Figlin R, de Kernion JB, Belldegrun A. Renal cell carcinoma: prognostic significance of incidentally detected tumors. J Urol 2000;163:426-30.
12. McLaughlin JK, Lipworth L, Tarone RE. Epidemiologic aspects of renal cell carcinoma. Semin Oncol 2006;33:527-33.
13. Martinez-Salamanca JI, Huang WC, Millan I, et al. Prognostic Impact of the 2009 UICC/AJCC TNM Staging System for Renal Cell Carcinoma with Venous Extension. Eur Urol.
14. Hunt JD, van der Hel OL, McMillan GP, Boffetta P, Brennan P. Renal cell carcinoma in relation to cigarette smoking: meta-analysis of 24 studies. Int J Cancer 2005;114:101-8.
15. Theis RP, Dolwick Grieb SM, Burr D, Siddiqui T, Asal NR. Smoking, environmental tobacco smoke, and risk of renal cell cancer: a population-based case-control study. BMC Cancer 2008;8:387.
16. Moore LE, Wilson RT, Campleman SL. Lifestyle factors, exposures, genetic susceptibility, and renal cell cancer risk: a review. Cancer Invest 2005;23:240-55.
17. Colli JL, Busby JE, Amling CL. Renal cell carcinoma rates compared with health status and behavior in the United States. Urology 2009;73:431-6.

18. Lee JE, Spiegelman D, Hunter DJ, et al. Fat, protein, and meat consumption and renal cell cancer risk: a pooled analysis of 13 prospective studies. J Natl Cancer Inst 2008;100:1695-706.
19. Lee JE, Hunter DJ, Spiegelman D, et al. Alcohol intake and renal cell cancer in a pooled analysis of 12 prospective studies. J Natl Cancer Inst 2007;99:801-10.
20. Dhote R, Thiounn N, Debre B, Vidal-Trecan G. Risk factors for adult renal cell carcinoma. Urol Clin North Am 2004;31:237-47.
21. Moyad MA. Review of potential risk factors for kidney (renal cell) cancer. Semin Urol Oncol 2001;19:280-93.
22. Lonser RR, Glenn GM, Walther M, et al. von Hippel-Lindau disease. Lancet 2003;361:2059-67.
23. Schmidt L, Junker K, Nakaigawa N, et al. Novel mutations of the MET proto-oncogene in papillary renal carcinomas. Oncogene 1999;18:2343-50.
24. Valladares Ayerbes M, Aparicio Gallego G, Diaz Prado S, Jimenez Fonseca P, Garcia Campelo R, Anton Aparicio LM. Origin of renal cell carcinomas. Clin Transl Oncol 2008;10:697-712.
25. Chow WH, Dong LM, Devesa SS. Epidemiology and risk factors for kidney cancer. Nat Rev Urol 2010;7:245-57.
26. Chow WH, Devesa SS, Warren JL, Fraumeni JF, Jr. Rising incidence of renal cell cancer in the United States. JAMA 1999;281:1628-31.
27. Fujita T, Iwamura M, Yanagisawa N, Muramoto M, Okayasu I, Baba S. Reclassification of the current tumor, node, metastasis staging in pT3 renal cell carcinoma. Int J Urol 2008;15:582-6.
28. Eggener S. TNM staging for renal cell carcinoma: time for a new method. Eur Urol 2010;58:517-9; discussion 9-21.
29. Butler BP, Novick AC, Miller DP, Campbell SA, Licht MR. Management of small unilateral renal cell carcinomas: radical versus nephron-sparing surgery. Urology 1995;45:34-40; discussion -1.
30. Chapman D, Moore R, Klarenbach S, Braam B. Residual renal function after partial or radical nephrectomy for renal cell carcinoma. Can Urol Assoc J;4:337-43.
31. Gleave ME, Elhilali M, Fradet Y, et al. Interferon gamma-1b compared with placebo in metastatic renal-cell carcinoma. Canadian Urologic Oncology Group. N Engl J Med 1998;338:1265-71.
32. Billiau A. Interferon: the pathways of discovery I. Molecular and cellular aspects. Cytokine Growth Factor Rev 2006;17:381-409.
33. Agarwala SS, Kirkwood JM. Interferons in the therapy of solid tumors. Oncology 1994;51:129-36.
34. Ferrantini M, Capone I, Belardelli F. Interferon-alpha and cancer: mechanisms of action and new perspectives of clinical use. Biochimie 2007;89:884-93.
35. Tomita S, Ishibashi K, Hashimoto K, et al. Suppression of SOCS3 increases susceptibility of renal cell carcinoma to interferon-alpha. Cancer Sci 2010.
36. Belardelli F, Gresser I. The neglected role of type I interferon in the T-cell response: implications for its clinical use. Immunol Today 1996;17:369-72.
37. Chen LK, Mathieu-Mahul D, Bach FH, Dausset J, Bensussan A, Sasportes M. Recombinant interferon alpha can induce rearrangement of T-cell antigen receptor

alpha-chain genes and maturation to cytotoxicity in T-lymphocyte clones in vitro. Proc Natl Acad Sci U S A 1986;83:4887-9.

38. Marumo K, Ueno M, Muraki J, Baba S, Tazaki H. Augmentation of cell-mediated cytotoxicity against renal carcinoma cells by recombinant interleukin 2. Urology 1987;30:327-32.
39. Dutcher J. Current status of interleukin-2 therapy for metastatic renal cell carcinoma and metastatic melanoma. Oncology (Williston Park) 2002;16:4-10.
40. Boccardo F, Rubagotti A, Canobbio L, et al. Interleukin-2, interferon-alpha and interleukin-2 plus interferon-alpha in renal cell carcinoma. A randomized phase II trial. Tumori 1998;84:534-9.
41. Ravaud A, Delva R, Gomez F, et al. Subcutaneous interleukin-2 and interferon alpha in the treatment of patients with metastatic renal cell carcinoma-Less efficacy compared with intravenous interleukin-2 and interferon alpha. Results of a multicenter Phase II trial from the Groupe Francais d'Immunotherapie. Cancer 2002;95:2324-30.
42. Culine S, Iborra F, Mottet N, et al. Subcutaneous interleukin-2 and interferon-alpha in metastatic renal cell carcinoma: results of a French regional experience in Languedoc. Am J Clin Oncol 2006;29:148-52.
43. Schindler C, Plumlee C. Inteferons pen the JAK-STAT pathway. Semin Cell Dev Biol 2008;19:311-8.
44. Mignogna C, Staibano S, Altieri V, et al. Prognostic significance of multidrug-resistance protein (MDR-1) in renal clear cell carcinomas: a five year follow-up analysis. BMC Cancer 2006;6:293.
45. Hanahan D, Weinberg RA. Hallmarks of cancer: the next generation. Cell 2011;144:646-74.
46. Cassavaugh J, Lounsbury KM. Hypoxia-mediated biological control. J Cell Biochem 2010.
47. Roodink I, Leenders WP. Targeted therapies of cancer: angiogenesis inhibition seems not enough. Cancer Lett 2010;299:1-10.
48. Roodink I, Leenders WP. Targeted therapies of cancer: angiogenesis inhibition seems not enough. Cancer Lett 2010;299:1-10.
49. D'Souza SS, Gururaj AE, Raj HM, Rossler J, Salimath BP. Inhibition of ascites tumor growth in vivo by sTie-2 is potentiated by a combinatorial therapy with sFLT-1. J Gene Med 2010.
50. Thomas M, Augustin HG. The role of the Angiopoietins in vascular morphogenesis. Angiogenesis 2009;12:125-37.
51. Stoeltzing O, Ahmad SA, Liu W, et al. Angiopoietin-1 inhibits vascular permeability, angiogenesis, and growth of hepatic colon cancer tumors. Cancer Res 2003;63:3370-7.
52. Stoeltzing O, Ahmad SA, Liu W, et al. Angiopoietin-1 inhibits tumour growth and ascites formation in a murine model of peritoneal carcinomatosis. Br J Cancer 2002;87:1182-7.
53. Skuli N, Simon MC. HIF-1alpha versus HIF-2alpha in endothelial cells and vascular functions: is there a master in angiogenesis regulation? Cell Cycle 2009;8:3252-3.

54. Corada M, Nyqvist D, Orsenigo F, et al. The Wnt/beta-catenin pathway modulates vascular remodeling and specification by upregulating Dll4/Notch signaling. Dev Cell 2010;18:938-49.
55. Ridgway J, Zhang G, Wu Y, et al. Inhibition of Dll4 signalling inhibits tumour growth by deregulating angiogenesis. Nature 2006;444:1083-7.
56. McMahon G. VEGF receptor signaling in tumor angiogenesis. Oncologist 2000;5 Suppl 1:3-10.
57. Luangdilok S, Box C, Harrington K, Rhys-Evans P, Eccles S. MAPK and PI3K signalling differentially regulate angiogenic and lymphangiogenic cytokine secretion in squamous cell carcinoma of the head and neck. Eur J Cancer 2010.
58. Ferrara N, Gerber HP, LeCouter J. The biology of VEGF and its receptors. Nat Med 2003;9:669-76.
59. Oommen S, Gupta SK, Vlahakis NE. Vascular endothelial growth factor - A (VEGF-A) induces endothelial and cancer cell migration through direct binding to integrin {alpha}9{beta}1: identification of a specific {alpha}9{beta}1 binding site. J Biol Chem 2010.
60. Roberts WG, Palade GE. Increased microvascular permeability and endothelial fenestration induced by vascular endothelial growth factor. J Cell Sci 1995;108 (Pt 6):2369-79.
61. Pekala P, Marlow M, Heuvelman D, Connolly D. Regulation of hexose transport in aortic endothelial cells by vascular permeability factor and tumor necrosis factor-alpha, but not by insulin. J Biol Chem 1990;265:18051-4.
62. Han FH, Li HM, Zheng DH, He YL, Zhan WH. The effect of the expression of vascular endothelial growth factor (VEGF)-C and VEGF receptor-3 on the clinical outcome in patients with gastric carcinoma. Eur J Surg Oncol 2010;36:1172-9.
63. Liao JK. Fine-tuning the angiogenic response to vascular endothelial growth factor. Circ Res 2008;103:229-30.
64. Bergers G, Brekken R, McMahon G, et al. Matrix metalloproteinase-9 triggers the angiogenic switch during carcinogenesis. Nat Cell Biol 2000;2:737-44.
65. Baeriswyl V, Christofori G. The angiogenic switch in carcinogenesis. Semin Cancer Biol 2009;19:329-37.
66. Norden AD, Drappatz J, Wen PY. Antiangiogenic therapies for high-grade glioma. Nat Rev Neurol 2009;5:610-20.
67. Baldewijns MM, van Vlodrop IJ, Vermeulen PB, Soetekouw PM, van Engeland M, de Bruine AP. VHL and HIF signalling in renal cell carcinogenesis. J Pathol 2010;221:125-38.
68. Andrae J, Gallini R, Betsholtz C. Role of platelet-derived growth factors in physiology and medicine. Genes Dev 2008;22:1276-312.
69. Yu JC, Li W, Wang LM, Uren A, Pierce JH, Heidaran MA. Differential requirement of a motif within the carboxyl-terminal domain of alpha-platelet-derived growth factor (alpha PDGF) receptor for PDGF focus forming activity chemotaxis, or growth. J Biol Chem 1995;270:7033-6.
70. Xiong W, Cheng BH, Jia SB, Tang LS. Involvement of the PI3K/Akt signaling pathway in platelet-derived growth factor-induced migration of human lens epithelial cells. Curr Eye Res 2010;35:389-401.

71. Perez J, Hill BG, Benavides GA, Dranka BP, Darley-Usmar VM. Role of cellular bioenergetics in smooth muscle cell proliferation induced by platelet-derived growth factor. Biochem J 2010;428:255-67.
72. Zachary I. VEGF signalling: integration and multi-tasking in endothelial cell biology. Biochem Soc Trans 2003;31:1171-7.
73. Bourbon NA, Yun J, Berkey D, Wang Y, Kester M. Inhibitory actions of ceramide upon PKC-epsilon/ERK interactions. Am J Physiol Cell Physiol 2001;280:C1403-11.
74. Rini BI, Small EJ. Biology and clinical development of vascular endothelial growth factor-targeted therapy in renal cell carcinoma. J Clin Oncol 2005;23:1028-43.
75. Brown MC, Cary LA, Jamieson JS, Cooper JA, Turner CE. Src and FAK kinases cooperate to phosphorylate paxillin kinase linker, stimulate its focal adhesion localization, and regulate cell spreading and protrusiveness. Mol Biol Cell 2005;16:4316-28.
76. Skalski M, Sharma N, Williams K, Kruspe A, Coppolino MG. SNARE-mediated membrane traffic is required for focal adhesion kinase signaling and Src-regulated focal adhesion turnover. Biochim Biophys Acta 2010.
77. Buettner R, Mesa T, Vultur A, Lee F, Jove R. Inhibition of Src family kinases with dasatinib blocks migration and invasion of human melanoma cells. Mol Cancer Res 2008;6:1766-74.
78. Guan JL. Role of focal adhesion kinase in integrin signaling. Int J Biochem Cell Biol 1997;29:1085-96.
79. Panetti TS. Tyrosine phosphorylation of paxillin, FAK, and p130CAS: effects on cell spreading and migration. Front Biosci 2002;7:d143-50.
80. Webb DJ, Donais K, Whitmore LA, et al. FAK-Src signalling through paxillin, ERK and MLCK regulates adhesion disassembly. Nat Cell Biol 2004;6:154-61.
81. Avruch J, Khokhlatchev A, Kyriakis JM, et al. Ras activation of the Raf kinase: tyrosine kinase recruitment of the MAP kinase cascade. Recent Prog Horm Res 2001;56:127-55.
82. Byrne AM, Bouchier-Hayes DJ, Harmey JH. Angiogenic and cell survival functions of vascular endothelial growth factor (VEGF). J Cell Mol Med 2005;9:777-94.
83. Sen P, Mukherjee S, Ray D, Raha S. Involvement of the Akt/PKB signaling pathway with disease processes. Mol Cell Biochem 2003;253:241-6.
84. Kennedy SG, Wagner AJ, Conzen SD, et al. The PI 3-kinase/Akt signaling pathway delivers an anti-apoptotic signal. Genes Dev 1997;11:701-13.
85. Brazil DP, Hemmings BA. Ten years of protein kinase B signalling: a hard Akt to follow. Trends Biochem Sci 2001;26:657-64.
86. Shaw RJ, Cantley LC. Ras, PI(3)K and mTOR signalling controls tumour cell growth. Nature 2006;441:424-30.
87. Karin M. Nuclear factor-kappaB in cancer development and progression. Nature 2006;441:431-6.
88. Dubrovska A, Kim S, Salamone RJ, et al. The role of PTEN/Akt/PI3K signaling in the maintenance and viability of prostate cancer stem-like cell populations. Proc Natl Acad Sci U S A 2009;106:268-73.

89. Blanco-Aparicio C, Renner O, Leal JF, Carnero A. PTEN, more than the AKT pathway. Carcinogenesis 2007;28:1379-86.
90. Gotink KJ, Verheul HM. Anti-angiogenic tyrosine kinase inhibitors: what is their mechanism of action? Angiogenesis 2010;13:1-14.
91. Hubbard SR, Miller WT. Receptor tyrosine kinases: mechanisms of activation and signaling. Curr Opin Cell Biol 2007;19:117-23.
92. Gross-Goupil M, Massard C, Ravaud A. Targeted therapies in metastatic renal cell carcinoma: overview of the past year. Curr Urol Rep 2012;13:16-23.
93. Zhang J, Yang PL, Gray NS. Targeting cancer with small molecule kinase inhibitors. Nat Rev Cancer 2009;9:28-39.
94. Mendel DB, Laird AD, Xin X, et al. In vivo antitumor activity of SU11248, a novel tyrosine kinase inhibitor targeting vascular endothelial growth factor and platelet-derived growth factor receptors: determination of a pharmacokinetic/pharmacodynamic relationship. Clin Cancer Res 2003;9:327-37.
95. Sulkes A. Novel multitargeted anticancer oral therapies: sunitinib and sorafenib as a paradigm. Isr Med Assoc J 2010;12:628-32.
96. Radulovic S, Bjelogrlic SK. Sunitinib, sorafenib and mTOR inhibitors in renal cancer. J BUON 2007;12 Suppl 1:S151-62.
97. Faivre S, Demetri G, Sargent W, Raymond E. Molecular basis for sunitinib efficacy and future clinical development. Nat Rev Drug Discov 2007;6:734-45.
98. Adams VR, Leggas M. Sunitinib malate for the treatment of metastatic renal cell carcinoma and gastrointestinal stromal tumors. Clin Ther 2007;29:1338-53.
99. Khosravan R, Toh M, Garrett M, et al. Pharmacokinetics and safety of sunitinib malate in subjects with impaired renal function. J Clin Pharmacol 2010;50:472-81.
100. Huang D, Ding Y, Li Y, et al. Sunitinib acts primarily on tumor endothelium rather than tumor cells to inhibit the growth of renal cell carcinoma. Cancer Res 2010;70:1053-62.
101. Finke JH, Rini B, Ireland J, et al. Sunitinib reverses type-1 immune suppression and decreases T-regulatory cells in renal cell carcinoma patients. Clin Cancer Res 2008;14:6674-82.
102. van Erp NP, Gelderblom H, Guchelaar HJ. Clinical pharmacokinetics of tyrosine kinase inhibitors. Cancer Treat Rev 2009;35:692-706.
103. Zhou SF. Drugs behave as substrates, inhibitors and inducers of human cytochrome P450 3A4. Curr Drug Metab 2008;9:310-22.
104. Motzer RJ, Hutson TE, Tomczak P, et al. Sunitinib versus interferon alfa in metastatic renal-cell carcinoma. N Engl J Med 2007;356:115-24.
105. Schrader AJ, Hofmann R. Metastatic renal cell carcinoma: recent advances and current therapeutic options. Anticancer Drugs 2008;19:235-45.
106. Gray LH, Conger AD, Ebert M, Hornsey S, Scott OC. The concentration of oxygen dissolved in tissues at the time of irradiation as a factor in radiotherapy. Br J Radiol 1953;26:638-48.
107. Shannon AM, Bouchier-Hayes DJ, Condron CM, Toomey D. Tumour hypoxia, chemotherapeutic resistance and hypoxia-related therapies. Cancer Treat Rev 2003;29:297-307.

108. Gray LH, Conger AD, Ebert M, Hornsey S, Scott OC. The concentration of oxygen dissolved in tissues at the time of irradiation as a factor in radiotherapy. Br J Radiol 1953;26:638-48.
109. Mees G, Dierckx R, Vangestel C, Van de Wiele C. Molecular imaging of hypoxia with radiolabelled agents. Eur J Nucl Med Mol Imaging 2009;36:1674-86.
110. Kurihara H, Honda N, Kono Y, Arai Y. Radiolabelled Agents for PET Imaging of Tumor Hypoxia. Curr Med Chem 2012;19:3282-9.
111. Fleckenstein W, Weiss C. A comparison of Po2 histograms from rabbit hind-limb muscles obtained by simultaneous measurements with hypodermic needle electrodes and with surface electrodes. Adv Exp Med Biol 1984;169:447-55.
112. Pacheco-Torres J, Lopez-Larrubia P, Ballesteros P, Cerdan S. Imaging tumor hypoxia by magnetic resonance methods. NMR Biomed 2010.
113. Shin HW, Cho CH, Kim TY, Park JW. Sunitinib deregulates tumor adaptation to hypoxia by inhibiting HIF-1alpha synthesis in HT-29 colon cancer cells. Biochem Biophys Res Commun 2010;398:205-11.
114. Hatzikirou H, Basanta D, Simon M, Schaller K, Deutsch A. 'Go or Grow': the key to the emergence of invasion in tumour progression? Math Med Biol 2010.
115. Semenza GL. Hypoxia-inducible factor 1 (HIF-1) pathway. Sci STKE 2007;2007:cm8.
116. Wu KL, Miao H, Khan S. JAK kinases promote invasiveness in VHL-mediated renal cell carcinoma by a suppressor of cytokine signaling-regulated, HIF-independent mechanism. Am J Physiol Renal Physiol 2007;293:F1836-46.
117. Nordsmark M, Bentzen SM, Rudat V, et al. Prognostic value of tumor oxygenation in 397 head and neck tumors after primary radiation therapy. An international multi-center study. Radiother Oncol 2005;77:18-24.
118. Krajewski KM, Giardino AA, Zukotynski K, Van den Abbeele AD, Pedrosa I. Imaging in renal cell carcinoma. Hematol Oncol Clin North Am 2011;25:687-715.
119. Choudhary S, Sudarshan S, Choyke PL, Prasad SR. Renal cell carcinoma: recent advances in genetics and imaging. Semin Ultrasound CT MR 2009;30:315-25.
120. Sacco E, Pinto F, Totaro A, et al. Imaging of renal cell carcinoma: state of the art and recent advances. Urol Int 2011;86:125-39.
121. Ueno D, Yao M, Tateishi U, et al. Early assessment by FDG-PET/CT of patients with advanced renal cell carcinoma treated with tyrosine kinase inhibitors is predictive of disease course. BMC Cancer 2012;12:162.
122. Rohren EM, Turkington TG, Coleman RE. Clinical applications of PET in oncology. Radiology 2004;231:305-32.
123. van Dongen GA, Visser GW, Lub-de Hooge MN, de Vries EG, Perk LR. Immuno-PET: a navigator in monoclonal antibody development and applications. Oncologist 2007;12:1379-89.
124. Kramer-Marek G, Capala J. The role of nuclear medicine in modern therapy of cancer. Tumour Biol 2012;33:629-40.
125. Vander Heiden MG, Cantley LC, Thompson CB. Understanding the Warburg effect: the metabolic requirements of cell proliferation. Science 2009;324:1029-33.
126. Raleigh JA, Dewhirst MW, Thrall DE. Measuring Tumor Hypoxia. Semin Radiat Oncol 1996;6:37-45.

127. Whitmore GF, Varghese AJ. The biological properties of reduced nitroheterocyclics and possible underlying biochemical mechanisms. Biochem Pharmacol 1986;35:97-103.
128. Krohn KA, Link JM, Mason RP. Molecular imaging of hypoxia. J Nucl Med 2008;49 Suppl 2:129S-48S.
129. Chapman JD, Franko AJ, Sharplin J. A marker for hypoxic cells in tumours with potential clinical applicability. Br J Cancer 1981;43:546-50.
130. Wiebe L.I MH. Imaging of Hypoxia: Tracer Developments: Kluwer Academic Publishers 1999.
131. Wiebe LI MA. Scintigraphic Imaging of Focal Hypoxic Tissue: Development and Clinical Applications of 123I-IAZA. Brazilian Arch Biol Technol 2002;45:S82-109.
132. Arabi M PM. Hypoxia PET/CT imaging: implications for radiation oncology. Q J Nucl Med Mol Imaging 2010;54:500.
133. Grierson JR, Link JM, Mathis CA, Rasey JS, Krohn KA. A radiosynthesis of fluorine-18 fluoromisonidazole. J Nucl Med 1989;30:343-50.
134. Mannan RH, Somayaji VV, Lee J, Mercer JR, Chapman JD, Wiebe LI. Radioiodinated 1-(5-iodo-5-deoxy-beta-D-arabinofuranosyl)-2-nitroimidazole (iodoazomycin arabinoside: IAZA): a novel marker of tissue hypoxia. J Nucl Med 1991;32:1764-70.
135. Kumar P SD, Xia H, McEwan AJB, Machulla HJ, Wiebe LI. Fluoroazomycin arabinoside (FAZA): Synthesis, 2H and 3H-labeling and preliminary biological evaluation of a novel 2-nitromidazole marker for tissue hypoxia. J Labelled Cpd Radiopharm 1999;42:3.
136. Postema EJ, McEwan AJ, Riauka TA, et al. Initial results of hypoxia imaging using 1-alpha-D: -(5-deoxy-5-[18F]-fluoroarabinofuranosyl)-2-nitroimidazole (18F-FAZA). Eur J Nucl Med Mol Imaging 2009;36:1565-73.
137. Lapi SE, Voller TF, Welch MJ. Positron Emission Tomography Imaging of Hypoxia. PET Clin 2009;4:39-47.
138. Holland JP, Lewis JS, Dehdashti F. Assessing tumor hypoxia by positron emission tomography with Cu-ATSM. The quarterly journal of nuclear medicine and molecular imaging : official publication of the Italian Association of Nuclear Medicine 2009;53:193-200.
139. Anderson CJ, Ferdani R. Copper-64 radiopharmaceuticals for PET imaging of cancer: advances in preclinical and clinical research. Cancer Biother Radiopharm 2009;24:379-93.
140. Taneja SS. Re: Metastatic renal cell carcinoma: relationship between initial metastasis hypoxia, change after 1 month's sunitinib, and therapeutic response: an 18F-fluoromisonidazole PET/CT study. J Urol 2012;187:1222-3.
141. Solomon B, Binns D, Roselt P, et al. Modulation of intratumoral hypoxia by the epidermal growth factor receptor inhibitor gefitinib detected using small animal PET imaging. Mol Cancer Ther 2005;4:1417-22.
142. Moore RB, Chapman JD, Mercer JR, et al. Measurement of PDT-induced hypoxia in Dunning prostate tumors by iodine-123-iodoazomycin arabinoside. J Nucl Med 1993;34:405-11.

143. Marcu L, Olver I. Tirapazamine: from bench to clinical trials. Curr Clin Pharmacol 2006;1:71-9.
144. Beck R, Roper B, Carlsen JM, et al. Pretreatment 18F-FAZA PET predicts success of hypoxia-directed radiochemotherapy using tirapazamine. J Nucl Med 2007;48:973-80.
145. Paez-Ribes M, Allen E, Hudock J, et al. Antiangiogenic therapy elicits malignant progression of tumors to increased local invasion and distant metastasis. Cancer Cell 2009;15:220-31.
146. Hugonnet F, Fournier L, Medioni J, et al. Metastatic renal cell carcinoma: relationship between initial metastasis hypoxia, change after 1 month's sunitinib, and therapeutic response: an 18F-fluoromisonidazole PET/CT study. J Nucl Med 2011;52:1048-55.
147. Matsumoto S, Batra S, Saito K, et al. Antiangiogenic agent sunitinib transiently increases tumor oxygenation and suppresses cycling hypoxia. Cancer Res 2011;71:6350-9.
148. Valable S, Petit E, Roussel S, et al. Complementary information from magnetic resonance imaging and (18)F-fluoromisonidazole positron emission tomography in the assessment of the response to an antiangiogenic treatment in a rat brain tumor model. Nucl Med Biol 2011;38:781-93.
149. Goel S, Duda DG, Xu L, et al. Normalization of the vasculature for treatment of cancer and other diseases. Physiol Rev 2011;91:1071-121.
150. Liu G, Jeraj R, Vanderhoek M, et al. Pharmacodynamic study using FLT PET/CT in patients with renal cell cancer and other solid malignancies treated with sunitinib malate. Clin Cancer Res 2011;17:7634-44.
151. Nagengast WB, Lub-de Hooge MN, Oosting SF, et al. VEGF-PET imaging is a noninvasive biomarker showing differential changes in the tumor during sunitinib treatment. Cancer Res 2011;71:143-53.
152. Gaustad JV, Simonsen TG, Leinaas MN, Rofstad EK. Sunitinib treatment does not improve blood supply but induces hypoxia in human melanoma xenografts. BMC Cancer 2012;12:388.
153. Ambrosini V, Quarta C, Zinzani PL, et al. 18[F]FDG small animal PET study of sorafenib efficacy in lymphoma preclinical models. The quarterly journal of nuclear medicine and molecular imaging : official publication of the Italian Association of Nuclear Medicine 2010;54:689-97.
154. Wuest M, Trayner BJ, Grant TN, et al. Radiopharmacological evaluation of 6-deoxy-6-[18F]fluoro-D-fructose as a radiotracer for PET imaging of GLUT5 in breast cancer. Nucl Med Biol 2011;38:461-75.
155. Reischl G, Dorow DS, Cullinane C, et al. Imaging of tumor hypoxia with [124I]IAZA in comparison with [18F]FMISO and [18F]FAZA--first small animal PET results. J Pharm Pharm Sci 2007;10:203-11.
156. Maier FC, Kneilling M, Reischl G, et al. Significant impact of different oxygen breathing conditions on noninvasive in vivo tumor-hypoxia imaging using [(1)(8)F]-fluoro-azomycinarabino-furanoside ([(1)(8)F]FAZA). Radiat Oncol 2011;6:165.
157. Piert M, Machulla HJ, Picchio M, et al. Hypoxia-specific tumor imaging with 18F-fluoroazomycin arabinoside. J Nucl Med 2005;46:106-13.

158. Murakami M, Zhao S, Zhao Y, et al. Evaluation of changes in the tumor microenvironment after sorafenib therapy by sequential histology and 18F-fluoromisonidazole hypoxia imaging in renal cell carcinoma. Int J Oncol 2012;41:1593-600.
159. Li L, Yu JM, Xing LG, et al. Hypoxic imaging with 99mTc-HL91 single photon emission computed tomography in advanced nonsmall cell lung cancer. Chin Med J (Engl) 2006;119:1477-80.
160. Sorger D, Patt M, Kumar P, et al. [18F]Fluoroazomycinarabinofuranoside (18FAZA) and [18F]Fluoromisonidazole (18FMISO): a comparative study of their selective uptake in hypoxic cells and PET imaging in experimental rat tumors. Nucl Med Biol 2003;30:317-26.
161. Lemasson B, Christen T, Serduc R, et al. Evaluation of the Relationship between MR Estimates of Blood Oxygen Saturation and Hypoxia: Effect of an Antiangiogenic Treatment on a Gliosarcoma Model. Radiology 2012;265:743-52.
162. Urtasun RC, Parliament MB, McEwan AJ, et al. Measurement of hypoxia in human tumours by non-invasive spect imaging of iodoazomycin arabinoside. Br J Cancer Suppl 1996;27:S209-12.
163. Kleiter MM, Thrall DE, Malarkey DE, et al. A comparison of oral and intravenous pimonidazole in canine tumors using intravenous CCI-103F as a control hypoxia marker. Int J Radiat Oncol Biol Phys 2006;64:592-602.
164. Khandani AH, Cowey CL, Moore DT, Gohil H, Rathmell WK. Primary renal cell carcinoma: relationship between 18F-FDG uptake and response to neoadjuvant sorafenib. Nucl Med Commun 2012;33:967-73.
165. Revheim ME, Roe K, Bruland OS, Bach-Gansmo T, Skretting A, Seierstad T. Monitoring the effect of targeted therapies in a gastrointestinal stromal tumor xenograft using a clinical PET/CT. Mol Imaging Biol 2011;13:1234-40.
166. Lyrdal D, Boijsen M, Suurkula M, Lundstam S, Stierner U. Evaluation of sorafenib treatment in metastatic renal cell carcinoma with 2-fluoro-2-deoxyglucose positron emission tomography and computed tomography. Nucl Med Commun 2009;30:519-24.
167. Vercellino L, Bousquet G, Baillet G, et al. 18F-FDG PET/CT imaging for an early assessment of response to sunitinib in metastatic renal carcinoma: preliminary study. Cancer Biother Radiopharm 2009;24:137-44.
168. Ueno D, Yao M, Tateishi U, et al. Early assessment by FDG-PET/CT of patients with advanced renal cell carcinoma treated with tyrosine kinase inhibitors is predictive of disease course. BMC Cancer 2012;12:162.
169. Amato RJ, Flaherty AL, Stepankiw M. Phase I trial of everolimus plus sorafenib for patients with advanced renal cell cancer. Clin Genitourin Cancer 2012;10:26-31.
170. Folkman J. Tumor angiogenesis: therapeutic implications. N Engl J Med 1971;285:1182-6.
171. Welti JC, Powles T, Foo S, et al. Contrasting effects of sunitinib within in vivo models of metastasis. Angiogenesis 2012;15:623-41.
172. Lu X, Kang Y. Hypoxia and hypoxia-inducible factors: master regulators of metastasis. Clin Cancer Res 2010;16:5928-35.

173. Conley SJ, Gheordunescu E, Kakarala P, et al. Antiangiogenic agents increase breast cancer stem cells via the generation of tumor hypoxia. Proc Natl Acad Sci U S A 2012;109:2784-9.
174. Fabian MA, Biggs WH, 3rd, Treiber DK, et al. A small molecule-kinase interaction map for clinical kinase inhibitors. Nat Biotechnol 2005;23:329-36.
175. Shinojima T, Oya M, Takayanagi A, Mizuno R, Shimizu N, Murai M. Renal cancer cells lacking hypoxia inducible factor (HIF)-1alpha expression maintain vascular endothelial growth factor expression through HIF-2alpha. Carcinogenesis 2007;28:529-36.
176. Sun J, Ahluwalia D, Lui Q, et al. Hypoxia-Activated Produg TH-302 Enhances Antitumor Activity of Antiangiogenics in Preclinical Models. In: American Association of Cancer Reseach 2011; Orlando, Florida; 2011.
177. Dorow DS, Cullinane C, Conus N, et al. Multi-tracer small animal PET imaging of the tumour response to the novel pan-Erb-B inhibitor CI-1033. Eur J Nucl Med Mol Imaging 2006;33:441-52.
178. Oswald J, Treite F, Haase C, et al. Experimental hypoxia is a potent stimulus for radiotracer uptake in vitro: comparison of different tumor cells and primary endothelial cells. Cancer Lett 2007;254:102-10.